

ALMA MATER STUDIORUM · UNIVERSITÀ DI BOLOGNA

Scuola di Scienze
Dipartimento di Fisica e Astronomia “Augusto Righi”
Corso di Laurea Magistrale in Fisica del Sistema Terra

Investigation on calving-tsunami sources in Jakobshavn Isbræ, Greenland

Relatore:
Dott. Filippo Zaniboni

Presentata da:
Manuel Stocchi

Anno Accademico 2019/2020

Abstract

In questo lavoro è stata testata l'efficacia di diverse sorgenti nel generare la condizione iniziale per simulare, tramite calcolo numerico, la propagazione di uno tsunami generato da un evento di calving. L'evento considerato è uno tsunami avvenuto il 21 agosto 2009 nel ghiacciaio di Jakobshavn Isbræ (nella costa Ovest della Groenlandia), a seguito di un calving ben documentato. La simulazione numerica è stata effettuata utilizzando il codice UBO-TSUFDF (creato e mantenuto dal gruppo di ricerca sugli tsunami dell'Università di Bologna), che utilizza uno schema di integrazione leapfrog con la tecnica delle staggered grids. Sono stati presi in esame tre diversi tipi di condizione iniziale: una gaussiana singola asimmetrica dipendente da tre parametri; una gaussiana doppia simmetrica dipendente da tre parametri; e una gaussiana doppia asimmetrica dipendente da quattro parametri. Per ogni sorgente sono state testate diverse combinazioni di valori dei parametri. La qualità delle simulazioni è stata valutata confrontando i mareogrammi virtuali con i dati raccolti da due mareografi situati in prossimità della località del calving. La valutazione è avvenuta principalmente confrontando polarità, ampiezza e tempo d'arrivo della prima perturbazione. Sono inoltre state confrontate le ampiezze spettrali dei dati con quelle delle simulazioni. Da queste analisi si è potuto constatare che le sorgenti a gaussiana doppia (sia simmetrica che asimmetrica) hanno prodotto risultati migliori della sorgente a gaussiana singola asimmetrica. Confrontando i risultati delle due sorgenti a gaussiana doppia non si sono riscontrate differenze significative. Pertanto, si conclude che tra le sorgenti investigate è da preferire la sorgente gaussiana doppia simmetrica, in quanto capace di garantire buoni risultati dipendendo da un minor numero di parametri.

Contents

1	Phenomenology of ice calving-generated tsunamis	3
1.1	Phenomenology of ice calving	3
1.1.1	Greenland ice sheet mass balance and sea level rise	4
1.1.2	Causes and models	5
1.2	Glacial earthquakes	7
1.3	Calving tsunamis	8
1.3.1	Impact of the calving style and volume upon tsunami waveform	9
1.3.2	Seiches and automatic detection of calving events	10
2	Tsunami dynamics	12
2.1	Newtonian fluids	12
2.2	Gravity waves	14
2.3	Non-linear shallow water theory	18
2.4	Numerical integration for tsunami propagation: the UBO-TSUFDF software	21
3	Case study and numerical setup	24
3.1	Case study: the August 21 st 2009 calving tsunami in Jakobshavn Isbræ	24
3.2	Simulation setup	32
3.3	Tested sources	37
4	Results and discussion	42
4.1	Best results	43
5	Conclusions	62
	Bibliography	67

Introduction

Earth is a complex system, emerging from the reciprocal interaction of its parts. Lithosphere, Hydrosphere, Atmosphere and Biosphere influence one another with a continuous and detailed exchange of mass and energy. Climate change is one of the results of these interactions, and probably the next big challenge humanity needs to face, as this evolution of the system may pose (and it's already posing) a serious threat to human life and economy. Glacier dynamics is one of the prominent aspects of climate change, and iceberg calving inserts within this context.

Iceberg calving is the detachment of (eventually large) portions glaciers into water. This phenomenon has been observed to generate tsunamis impacting upon near coasts. The study of calving tsunamis has developed only in the beginning of 2000s, and so it's a pretty young field when compared to earthquake or landslide tsunamis. The understanding of this phenomenon could result in improvements in both the long-term run of modeling ice dynamics (and thus climate change) and in the more immediate study of tsunami hazard for local population.

The aim of this work is to model different kinds of source shape-functions for iceberg calving tsunamis, in particular considering a well documented event happened on August 21st 2009 in Jakobshavn Isbræ, in Western Greenland. The hope is to produce a piece of information that will insert in the bigger frame of calving modeling: as happens in seismology and other fields, the knowledge of a source can make possible inversion procedures and lead to information regarding the causes of these events. In chapter 1 the phenomenology of iceberg calving and related tsunamis, according to the current knowledge of the phenomenon will be described. Chapter 2 will show the physics of tsunami description and modeling and will present UBO-TSUFDF, the software used in this work to simulate tsunami propagation. Chapter 3 will describe the case study and methods that have been used to conduct this work. Chapter 4 will present and discuss the results of this work.

Chapter 1

Phenomenology of ice calving-generated tsunamis

In this chapter the phenomenological aspects of ice calving and calving-induced tsunamis will be discussed. In sect. 1.1 the phenomenon of ice calving is presented and studied, along with its impact on sea level rise. In sect.1.2 will be described the phenomenon of glacial earthquakes, one of the most important consequences of ice calving. In sect. 1.3 will be exposed the phenomenon of calving-induced tsunamis, according to the most recent knowledge about the phenomenon.

1.1 Phenomenology of ice calving

Ice calving (also known as iceberg calving or glacier calving) is a phenomenon in which ice shelves or termini of glaciers discharge large volumes of ice directly into water, generating icebergs. These events play a fundamental role in the total ice mass balance of polar regions, and particularly in Greenland, but despite its importance, their dynamics is still not well known: the description demands accounting for both thermodynamic and mechanical properties of glaciers, and data gathering is often hard because of the intrinsic inaccessibility of these places. Moreover, interest over calving detection systems has developed only in the last two decades, along with the overall growing interest in environmental issues. There are several reports of calving events generating tsunamis (both terrific and interesting videos can be easily found on YouTube or other content sharing platforms). This is both a problem and a solution: it is a problem, because tsunamis can cause several human and economical damages. It is a solution, because the detection of tsunami waves can be used to reveal iceberg calving events, thus leading to a better understanding of the problem.

Study	Method	Period	Results (km ³ yr ⁻¹)
Rignot 2006	Glacier discharge estimate	1996	-56 ± 30
Rignot 2006	Glacier discharge estimate	2000	-92 ± 30
Rignot 2006	Glacier discharge estimate	2005	-167 ± 40
Thomas 2006	Altimetry variation analysis	1993-1999	-29 ± 25 ^b
Thomas 2006	Altimetry variation analysis	1998-2004	-88 ± 26 ^b
Velicogna 2006	Gravimetric analysis	2002-2006	-248 ± 36
Broeke 2009	Surface mass balance-discharge estimate	2000-2008	-181 ^b
Mouginot 2019	Several ^a	1972-1980	+51 ± 23 ^b
Mouginot 2019	Several	1980-1990	-57 ± 19 ^b
Mouginot 2019	Several	1990-2000	-48 ± 19 ^b
Mouginot 2019	Several	2000-2010	-204 ± 19 ^b
Mouginot 2019	Several	2010-2018	-312 ± 22 ^b

Table 1.1: GrIS mass loss according to several studies, carried out with different methods. Study *Rignot 2006* refers to Rignot and Kanagaratnam 2006. Study *Thomas 2006* refers to Thomas et al. 2006. Study *Velicogna 2006* refers to Velicogna and Wahr 2006. Study *Broeke 2009* refers to Broeke et al. 2009. Study *Mouginot 2019* refers to Mouginot et al. 2019.

^a Due to the large period spanned by the Mouginot et al. 2019 study, several data samples, obtained in different ways, have been used. See the full work for more informations.

^b Original published value in Gt yr⁻¹, converted into km³ yr⁻¹ for consistency, using $\rho = 917 \text{ Kg m}^{-3}$ for ice density.

1.1.1 Greenland ice sheet mass balance and sea level rise

Among all the ways polar regions can lose ice mass, calving events are the most direct ones. This holds true for both arctic and antarctic regions. We will mainly focus on Greenland.

Several studies have been carried out in order to quantify and understand the mass balance of Greenland ice sheet (GrIS). Quantification of this quantity has been performed in different ways and gave different results as can be seen in table 1.1. All of these studies, although disagreeing upon values, suggest an acceleration in mass loss occurred over the last two decades. Moreover, some of these studies suggest that most of this loss concerns the southern portion of GrIS. It is also possible to calculate how much of the sea level rise is due to the GrIS mass loss: e.g. Broeke et al. 2009 estimates a contribution 0.46 mm yr⁻¹ in the 2000-2008 period. Other studies also report values in the range 0.5 – 1 mm yr⁻¹ (see Velicogna and Wahr 2006).

Of particular interest for our purpose is the partition of GrIS mass loss between different factors. A typical ice mass budget model is the SMB-D (*Surface Mass Balance - Discharge*) in which two particular components are identified: the surface mass balance (SMB), that accounts for positive contributions due to snowfall and negative contributions due to runoff; and Discharge (D), that is the negative contribution due to the discharge of ice into water, via calving events and retreat of the glacier termini. According to Broeke et al. 2009, ice discharge, and thus calving, has a leading role in the total mass balance of GrIS.

1.1.2 Causes and models

The complete description of calving processes has proved to be hard to depict. As reported in Benn and Åström 2018, calvings form from the propagation of fractures within the glacier. Rheology of ice strongly depends upon the time scale of interest, as over long times ice can be treated as a non-Newtonian fluid (i.e. stress does not depend linearly from strain rate), while over shorter time scales the rheology can be considered as elastic-brittle, i.e. once a stress component τ reaches a limit value τ_{max} the ice breaks generating fractures. The exact value of τ_{max} for ice is not exactly known, as it may depend upon several properties that may largely vary from one glacier to another, such as temperature, crystal anisotropy, presence of debris, impurity and others. In particular, the dependence of rheology upon temperature suggests that the rise of global mean sea and air temperature may be a concurring cause in the growth of ice mass loss in Greenland (as well as in other polar regions). As reported by Benn and Åström 2018 τ_{max} for tensile stresses is in the 90 – 400 kPa range and higher for shear stresses. Thus, a roughly isotropic stress field tends to generate more tensile than shear fractures. Tensile fractures in a glacier are commonly known as *crevasses*. The pressure of the water penetrating within the crevasse offers additional tensile stress to help propagate the fracture. This may happen both in surface or basal crevasses, specially in floating glaciers. If a crevasse penetrates enough to break the full thickness of a glacier, calving occurs. In order for this to happen, fractures are needed to grow and propagate, and this is not granted: often tensile stresses within the glaciers are not high enough, and fractures will stabilize.

As still pointed out by Benn and Åström 2018, the presence of damage (that is, the overall presence of crevasses and micro-scale fractures) highly impacts glacier dynamics, altering its rheology: as damaged parts are no more able to bear stresses, ice viscosity and Young modulus decrease linearly with damage, as presented in Sun et al. 2017. Although it is an important process, Benn and Åström 2018 reports that there are not sufficient data to fully comprehend this complex problem.

Calving often happens in floating or almost-floating glacier termini: buoyant forces and ice-water heat transfer play a significant role in triggering calvings. Benn et al. 2007 identifies four different calving processes. Naming follows Benn and Åström 2018.

1. **Longitudinal extension:** consists in the full size detachment of ice shelves, and is typically caused by longitudinal extension of the glacier termini. This typically happens when a grounded glacier has a floating terminus. The difference between lithostatic stresses at the grounded base and buoyant forces at the terminus creates a non-zero total torque distribution that will eventually lead to the detachment of the ice front. This is the typical process of ice calving happening in Antarctica, causing the release of large floating ice shelves.
2. **Melt undercutting:** consists in the undercutting of sub-aerial ice fronts due to sub-aqueous melting. When mechanical or thermodynamic processes melt the base of a tidewater ice cliff, the weight of the sub-aerial part of the cliff is no longer supported. This generates an unbalanced torque that may lead to calving. This process is believed to be dominant in warm water-terminating glaciers, as in fjords in summer (Benn and Åström 2018).
3. **Buoyant calving - ice foot:** consist in the undercutting of the sub-aqueous ice foot due to sub-aqueous melting. Glaciers flowing underwater may have sections (Benn and Åström 2018 reports even hundreds of meters) of ice way below their buoyant equilibrium depth. In this way, buoyant forces can generate eccentric stresses that may lead to the detachment of the ice tongue. Benn and Åström 2018 reports that this one of the main calving processes happening in Greenland's fast-flowing tidewater glaciers.
4. **Buoyant calving - full thickness:** this is analogous to the previous one, but affects the full-thickness of the glacier front. Water-terminating glaciers may have crevasses at its base. Bouyant forces, aided by the pressure of water entering basal crevasses, may lead to non-zero torques past these crevasses, leading to the full-thickness capsizing of the glacier tongue.

The growing interest upon climatic issues has developed a need for finer climatic models, and finer climatic models have to account for the cryosphere-hydrosphere interaction via calving. To achieve this, good evaluations of calving rates (i.e. glacier mass or volume loss due to calving) are needed.

In general, a proper mechanical model capable of predicting calving rates with an acceptable precision is missing; also, model validation is hindered by the lack of precise ice rheology models and difficult data collection. In time studies focused more on a statistical description of calving events, via the so-called *calving laws*. A calving law is an empirical equation relating the calving speed v_c (i.e. the glacier length lost due to calving, typically measured in m yr^{-1}) with other measurable quantities, such as water temperature and depth, ice thickness, accumulated strain etc. For example, Brown et al. 1982 proposed a simple calving law for the Columbia Glacier (Alaska): $\bar{v}_c = c\bar{h}_w$, where \bar{v}_c is the calving speed (averaged over the glacier width), \bar{h}_w is the water depth at the

terminus (averaged over the glacier width) and $c = 27(2) \text{ yr}^{-1}$. Other examples of calving laws may be found in Alley et al. 2008 and Veen 2002. Calving laws have inherent issues: being empirical relations, they present not clear insight upon the physical mechanisms that generate calving. Moreover, the validity of these laws is often limited to a particular glacier and to a particular time span, as a change in the calving mechanism (as Walter et al. 2010 reports has happened for Columbia Glacier in 2007) may hinder the validity of the law. A more general approach has been carried out by Bassis 2011: in this work, the glacier terminus is considered to be a point particle performing a 1-dimensional random walk, and this allows to find approximate calving laws for different calving regimes. Still this method offers little insight about the core mechanisms of the calving process. When a calving event occurs, the detachment of the ice block has two main consequences: 1) a glacial earthquake (commonly known as "icequake") occurs; 2) an iceberg is released, which plunging into water or by capsizing may cause a tsunami.

1.2 Glacial earthquakes

Glacial earthquakes are earthquakes that show large magnitudes (roughly $M5.0$), are detectable only at teleseismic distances with long-period (tens - hundreds of seconds, roughly and order of magnitude greater than the typical duration of tectonic earthquakes of similar magnitude) surface waves and whose sources have a spatial distribution highly correlated with glacial areas (Greenland, Alaska, Antarctica). This phenomenon was firstly reported by Ekström et al. 2003. The most important characteristics of glacial earthquakes have been summarized from Ekström et al. 2003, Ekström 2006, Tsai and Ekström 2007, Joughin et al. 2008a by Tsai et al. 2008: these earthquakes have sources at calving fronts of fast-flowing ($\geq 1 \text{ km yr}^{-1}$) glaciers; with a source mechanism well described by a force distribution directed roughly along the glacial flow, surface wave magnitude in the range $4.6 \leq M_{sw} \leq 5.1$; high spectral energy density in the 20 – 100 s; high seasonality (the number of events positively correlates with local temperature and presence of ice mélange); high variability of the source position within the same outlet glacier; they have characteristic amplitudes depending upon the source glacier; and, most noticeable, the number of glacial earthquakes is higher in glacier retreat periods (summer in northern hemisphere, winter in southern hemisphere), when more calvings occur.

Tsai et al. 2008 proposed that glacial earthquakes may be due to the calving of large icebergs capsizing near to the glacial front. More evidences were brought by Nettles et al. 2008, that reports a coincidence between glacial earthquakes, major ice calving events and step-wise changes in glacier flow speed Heleim Glacier (Greenland); and Nettles and Ekström 2010, that reports high correlation between glacial earthquakes and large (cubic-kilometers scale) calving events in the 2000-2008 period in Greenland and Antarctica. More evidence has been brought by Joughin et al. 2008a, Amundson et al. 2008 and Veicht and Nettles 2012, so it is possible to trace a cause-effect relation between calving

and glacial earthquakes with a good degree of safety.

Glacial earthquakes may represent a good opportunity in understanding the mechanism of calving. As can be done with any earthquake, the signal of glacial earthquakes can be inverted to obtain a source function, from which information about the calving process could be inferred. Since from the first inversions performed by Ekström et al. 2003, it's been noticed that better results were found with single-force source functions (used for the inversion of landslide earthquakes) rather than with moment-tensor source functions (typically used for tectonic earthquakes). In particular, the source function that gave best results in Ekström et al. 2003 (one earthquake occurred in Alaska, 4 September 1999 15:15:20.0) and Tsai and Ekström 2007 (184 earthquakes in Greenland, from 1993 to 2005) is the Centroid Single Force function (CSF), defined in Kawakatsu 1989 (see 1.1). These kind of sources are often used for modeling landslide earthquakes, and their analysis can give information about the source mechanism: as claimed in Kawakatsu 1989 the two-fold time integration of the source moment force leads to a parameter that can be interpreted as the product of of the sliding mass and the run-out. Applying the same idea to a glacial earthquake occurred in Dall glacier (Alaska, 4 September 1999, 15:15:20.0) Ekström et al. 2003 found this parameter to be $1.3 \times 10^{14} \text{kg m}$, that can be interpreted e.g. as a volume of 10 km^3 of mass sliding for 13 m

1.3 Calving tsunamis

The subaerial flow of large masses (Walder et al. 2003 reports landslides, rockfalls, debris avalanches, debris flows and pyroclastic flows) into water can have various effects, among which there is the generation of large, long period tsunami waves. This kind of event has been observed both in ocean and lake waters. Large ice blocks calving into water also generate tsunami waves. Observations of these events are relatively common, given that many glaciers are considered tourist attractions and are therefore often visited, but all of these observations often lack in detail and useful scientific information. Data concerning iceberg calving are far more rare, as these kind of events happen without clear prior indications and in often unsurveyed areas. Even if many (Amundson et al. 2008, Amundson et al. 2010 among

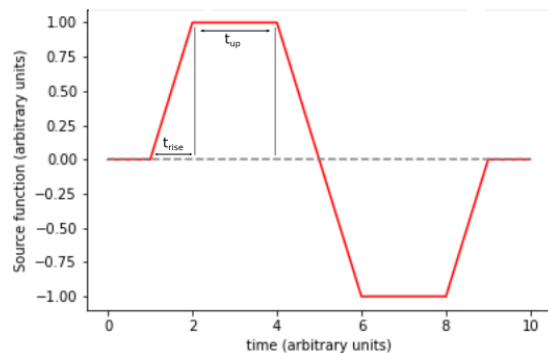


Figure 1.1: Simmetric centroid single force (CSF) function, as presented by Kawakatsu 1989, plotted in arbitrary adimensional units.

others) mentioned calving tsunamis before, one of the first direct measurements of these kind of tsunamis are due to Marchenko et al. 2012, that used pressure and temperature recorders to observe a tsunami wave near Temple Fjord (Spitsbergen, Svalbard Islands, Norway). Other recordings followed, both in arctic and antarctic regions. One of the most detailed observations is due to Lüthi and Vieli 2016, that observed and collected data from a calving event in Equip Sermia (West Greenland) happened in July 2014 using several methods. These observations allowed testing of previous and successive theoretical models and numerical simulations.

1.3.1 Impact of the calving style and volume upon tsunami waveform

As it is easy to assume, bigger calving volumes produce waves with greater amplitude. A study conducted by Minowa et al. 2019 in Bowdoin Glacier (Northwestern Greenland) found a positive correlation between maximal wave amplitude H_{max} and calving volume V_c , finding the following relation:

$$V_c = (1.3 \times 10^5 \text{m}^2)H_{max} - 9.3 \times 10^3 \text{m}^3 \quad (1.1)$$

It is possible that the values of the parameters appearing in (1.1) are characteristic of the site and thus not universal. Still, the presence of a linear relation between calved volume and tsunami wave amplitude grants an additional tool in estimating calving fluxes.

Moreover, calving style plays an important role in the determination of the properties of the generated tsunami wave. Heller et al. 2019 conducted large scale experiments to study the difference in tsunamigenic potential of different calving mechanisms. Within an artificial basin set up with an array of pressure gauges, a block of known dimension has been used to generate tsunamis within the basin, reproducing five different ideal calving styles: A) capsizing; B) gravity-driven fall; C) Buoyancy-driven fall; D) gravity-driven overturning; E) Buoyancy-driven overturning. A schematic representation of these calving styles is reported in Fig. 1.2. This experiment led to several main conclusions:

1. The calving process releases potential (gravitational and buoyant) energy into water, generating a wave;
2. Different calving styles result in different waveforms;
3. Wave amplitude depends upon the calving style, with gravity-dominated mechanisms such as B and D resulting in generating roughly one order of magnitude higher waves than mechanisms A,C, E;
4. After the initial wave, a tsunami train (i.e. a long lasting signal of non-linear waves with smaller amplitude) is released, due to fluctuations and tilting of the block;

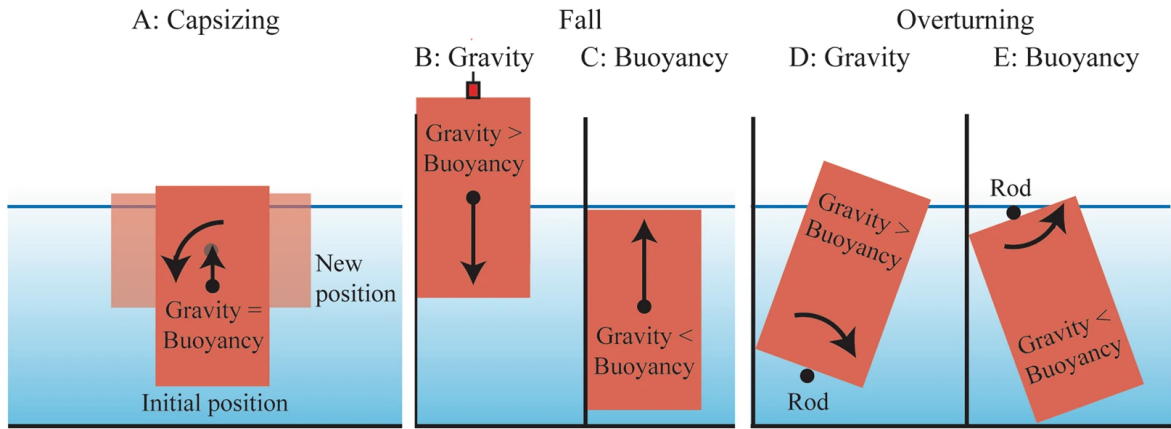


Figure 1.2: Schematic representation of the different calving styles reproduced in Heller et al. 2019. Image taken and modified from Heller et al. 2019.

5. Landslide-tsunami models can predict well the height of gravity-dominated tsunamis.

Even if capsizing calvings seem to produce smaller tsunamis, several recordings of destructive tsunamis are due to capsizing events. As these events may happen close to harbors and fjords, resonance effects (not observed by Heller et al. 2019) as well as vicinity between structures and tsunami sources, can still cause destructive tsunamis.

1.3.2 Seiches and automatic detection of calving events

As widely known from basic wave theory, waves in bound domains create standing waves: generally speaking, a standing wave can be seen as the superimposition of all the possible natural modes of the waves; these modes have periods and frequencies that depend uniquely upon the geometry of the domain and the propagation medium. Sources within the closed domain can excite particular natural modes of a system, thus generating standing waves within the domain. In general, different sources tend to excite different modes.

As for water waves, basins as harbors, ports or gulf can be fairly treated as bound domains and thus allow the formation of standing waves, known as *seiches*. External sources (e.g. a boat sailing within an harbor) are capable of exciting particular modes within a basin. Even tsunamis can excite seiches within (partially-)enclosed basins, in particular exciting long period and large wavelength standing waves, often with high amplitude (the word *tsunami* itself can be translated from japanese as "harbor wave"). It is straightforward to assume that calving tsunamis generating within almost-closed basins as fjords can excite seiches. These waves, upon impacting against the shore, generate a periodic low frequency ($\sim 10^{-3}$ Hz) surface wave seismic signal that can be detected by seismometers.



Figure 1.3: Disko bay (*Qeqertarsuup tunua* in Greenlandic; *Diskobugten* in Danish). This bay can be considered as a closed basin in most applications, allowing the formation of seiches. Jakobshavn Isbræ is also shown, towards East. Image taken and modified from Google Earth (<https://earth.google.com>)

The Greenland Ice Sheet Monitoring Network project (GLISN, Dahl-Jensen et al. 2010), that placed an array of broadband seismometers in several locations all over Greenland, allows continuous measurements of seismic signals, allowing to observe several events of calving tsunamis exciting seiches. As reported by Amundson et al. 2012, calving events happening inside Jakobshavn Isbræ can excite seiches within the fjord and in Disko Bay (see fig. 1.3). On the other side, Walter et al. 2013 used seismic data to automatically detect calving events, by looking for seiches signals. Automatic detection algorithms like the one of Walter et al. 2013 allows the recording of (almost) every calving event happening within an area, and thus are fairly useful instruments.

Chapter 2

Tsunami dynamics

For our purposes, the best way to describe ocean water is the model of the *newtonian fluid*. In this chapter all the basic notions of continuum mechanics will be considered as known and the notions of *strain* ϵ_{ij} , *strain rate* $\dot{\epsilon}_{ij}$, *traction* T_i and *stress* τ_{ij} will be used without a previous definition. All the definitions and properties of these quantities can be found in any continuum mechanics text (see, for example, Spencer 1980). In sect. 2.1 all the basic notions and relations of fluid dynamics will be exposed. In sect. 2.2 the theory of gravity waves will be presented. Sect. 2.3 will present the non-linear shallow water theory, that is the theoretical frame in which tsunami propagation models develop. Sect. 2.4 presents and explains the UBO-TSUF code, used in this work to simulate tsunami propagation.

2.1 Newtonian fluids

The results presented in this section will be given without demonstration. The sources for these results, along with their demonstrations, can be found in Batchelor 1967, Elmore and Heald 1969 and Guyon et al. 2001.

Continuity equation

The law of conservation of mass for a fluid continuum is given by the *continuity equation*:

$$\frac{1}{\rho} \frac{d\rho}{dt} + \frac{\partial v_j}{\partial x_j} = 0 \quad (2.1)$$

In most cases the variations of density can be neglected. This is the *Boussinesq approximation*, and in this case (2.1) simplifies into

$$\frac{\partial v_k}{\partial x_k} = 0 \quad (2.2)$$

When (2.2) holds the fluid is called *incompressible*.

The Boussinesq approximation holds without issues for the typical oceanic gravity waves problem, so from now on we will be considering our fluids as incompressible.

Constitutive equation

The constitutive equation of an isotropic *Newtonian fluid* is

$$\tau_{ij} = -p\delta_{ij} + 2\eta \left(\dot{\epsilon}_{ij} - \frac{1}{3}\epsilon_{kk}\delta_{ij} \right) \quad (2.3)$$

where p is the thermodynamic pressure, and η is the dynamic viscosity of the fluid. If the fluid is incompressible, (2.2) implies $\epsilon_{kk} = 0$, so (2.3) simplifies into

$$\tau_{ij} = -p\delta_{ij} + 2\eta\dot{\epsilon}_{ij} \quad (2.4)$$

Vorticity and velocity potential

The vorticity ω_i of a fluid is defined by

$$\omega_i = \frac{1}{2}e_{ijk} \frac{\partial v_k}{\partial x_j} \quad (2.5)$$

and represents the angular velocity of the fluid near a particular point. In many cases a fluid can be considered *irrotational*, i.e. $\omega_i = 0$, and thus v_i can be expressed as the gradient of a scalar potential, the *velocity potential* ϕ :

$$v_i = \frac{\partial \phi}{\partial x_i} \quad (2.6)$$

Navier-Stokes equation

The equation of motion for a continuum is:

$$\rho \frac{\partial v_i}{\partial t} = f_i + \frac{\partial \tau_{ij}}{\partial x_j} \quad (2.7)$$

where f_i represents the body forces acting on the medium. Assuming that the only body force acting on the medium is the gravitational pull (so $f_i = \rho g_i$, with g_i being gravitational acceleration) and that the medium is an incompressible isotropic Newtonian fluid with constitutive equation given by (2.4), we obtain the *Navier-Stokes equation*:

$$\rho \left(\frac{\partial v_i}{\partial t} + v_j \frac{\partial v_i}{\partial x_j} \right) = \rho g_i - \frac{\partial p}{\partial x_i} + \eta \frac{\partial^2 v_i}{\partial x_j \partial x_j} \quad (2.8)$$

Bernoulli equation

The law of conservation of energy for an irrotational incompressible inviscid fluid under a body force potential Ω is expressed by the *Bernoulli equation*:

$$\frac{\partial\phi}{\partial t} + \frac{1}{2}v^2 + \int \frac{dp}{\rho} + \Omega = f(t)$$

where ϕ is the velocity potential, $\frac{1}{2}v^2$ is the kinetic energy (for the unit mass) and $f(t)$ is an integration constant (with respect to spatial coordinates) that in most cases can be set to zero. This leads to the form of Bernoulli equation that will be used in the next section:

$$\frac{\partial\phi}{\partial t} + \frac{1}{2}v^2 + \int \frac{dp}{\rho} + \Omega = 0 \quad (2.9)$$

2.2 Gravity waves

Gravity waves are waves propagating in a fluid medium, in which gravity acts as restoring force. We will now study the propagation of gravity waves in the boundary between water and air. Water will be considered as an incompressible inviscid irrotational fluid, with homogeneous density ρ filling an infinitely wide basin of depth H . The surface tension will be neglected and we will only consider waves of small amplitude. The problem is bi-dimensional, so we choose a frame of reference with the x axis in the direction of the wave propagation and the z axis pointing upwards. The origin is set on in the equilibrium position of the free surface. Let $\eta(x, t)$ be the perturbation of the free surface. For the sake of simplicity we denote $v_x = u$ and $v_y = w$.

Because of the fluid being irrotational we can use the velocity potential (2.6):

$$u = \frac{\partial\phi}{\partial x}; \quad w = \frac{\partial\phi}{\partial z} \quad (2.10)$$

Due to the fluid being incompressible, inserting (2.6) in (2.2) leads to

$$\frac{\partial^2\phi}{\partial x^2} + \frac{\partial^2\phi}{\partial z^2} = 0 \quad (2.11)$$

that is the *Laplace equation*. In order to solve it we need a set of boundary conditions.

At the bottom of the basin, we set

$$\frac{\partial\phi}{\partial z} = 0 \quad \text{in } z = -H \quad (2.12)$$

This boundary condition forces water not to leave or cross the bottom of the basin. At the free surface, we set

$$\frac{d\eta}{dt} = \frac{\partial\eta}{\partial t} + u\frac{\partial\eta}{\partial x} = \frac{\partial\phi}{\partial z} \quad \text{in } z = \eta$$

In the limit of small amplitudes $u \frac{\partial \eta}{\partial x}$ can be neglected. In addition, this limit allows us to write

$$\left. \frac{\partial \phi}{\partial z} \right|_{z=\eta} \approx \left. \frac{\partial \phi}{\partial z} \right|_{z=0} + \eta \left. \frac{\partial^2 \phi}{\partial z^2} \right|_{z=0}$$

where the second term on right hand side can be neglected. So our second boundary condition turns into

$$\frac{\partial \eta}{\partial t} \approx \frac{\partial \phi}{\partial z} \quad \text{in } z \approx 0 \quad (2.13)$$

Boundary conditions (2.12) and (2.13) are often called *cinematic conditions* due to their purpose to “limit” the motion of the particles of the fluid. Another boundary condition, following from the balance of forces in the fluid, is the so called *dynamic condition*. This follows directly from the Bernoulli equation (2.9), that we can rewrite as

$$\frac{\partial \phi}{\partial t} + \frac{1}{2}(u^2 + w^2) + \int \frac{dp}{\rho} + gz = 0$$

where Ω has been expressed as gz . The kinetic energy term can be neglected in the limit of small perturbations, leading to

$$\frac{\partial \phi}{\partial t} + \frac{\Delta p}{\rho} + gz = 0$$

where Δp is the difference between the $p(z)$ and the atmospheric pressure $p_0 = p(z = \eta)$. So at $z = \eta$ we have that $\Delta p = 0$, and using the same approximation used in (2.13) we obtain

$$\left. \frac{\partial \phi}{\partial t} \right| + g\eta = 0 \quad (2.14)$$

So the problem we have to solve is given by (2.11) (and (2.10)) with boundary conditions (2.12), (2.13) and (2.14):

$$\begin{cases} u = \frac{\partial \phi}{\partial x}, & w = \frac{\partial \phi}{\partial z} \\ \frac{\partial^2 \phi}{\partial x^2} + \frac{\partial^2 \phi}{\partial z^2} = 0 \\ \frac{\partial \phi}{\partial z} = 0 & \text{in } z = -H \\ \frac{\partial \eta}{\partial t} \approx \frac{\partial \phi}{\partial z} & \text{in } z \approx 0 \\ \left. \frac{\partial \phi}{\partial t} \right| + g\eta = 0 \end{cases} \quad (2.15)$$

Solution for a harmonic perturbation

Let us consider a harmonic perturbation like

$$\eta(x, t) = a \cos(kx - \omega t) \quad (2.16)$$

This is not restrictive at all, given that every real perturbation can be expanded in a Fourier series and that (2.11) is linear. The boundary conditions of (2.15) suggest that the dependences of ϕ on x and t must be sinusoidal. So our solution has the form:

$$\phi(z, x, t) = f(z) \sin(kx - \omega t) \quad (2.17)$$

Inserting (2.17) in (2.11) we obtain

$$\frac{\partial^2 f(z)}{\partial z^2} - k^2 f(z) = 0$$

that has solution in the form

$$f(z) = Ae^{kz} + Be^{-kz} \quad (2.18)$$

Using BCs (2.12) and (2.13) we can easily obtain the values for A and B

$$A = \frac{a\omega}{2k} \frac{e^{kH}}{\sinh kH} \quad B = \frac{a\omega}{2k} \frac{e^{-kH}}{\sinh kH}$$

that leads to the solution

$$\phi(x, z, t) = \frac{a\omega}{k} \frac{\cosh k(H+z)}{\sinh kH} \sin(kx - \omega t) \quad (2.19)$$

Thus the velocities u and w are (from (2.10)):

$$u = a\omega \frac{\cosh k(H+z)}{\sinh kH} \cos(kx - \omega t) \quad w = a\omega \frac{\sinh k(H+z)}{\sinh kH} \sin(kx - \omega t) \quad (2.20)$$

These two solutions are plotted in fig.???. So, (2.19) is the solution of the problem. If we insert it in the dynamic boundary condition (2.14) we obtain the *dispersion relation* of gravity waves:

$$\omega^2 = \frac{gk}{\tanh kH} \quad (2.21)$$

that is not linear, so gravity waves are *dispersive*. As known from general wave theory we can obtain the *phase velocity* c and the *group velocity* c_g via the relations

$$c = \frac{\omega}{k} \quad c_g = \frac{\partial \omega}{\partial k}$$

Using (2.21) we obtain

$$c = \sqrt{\frac{g}{k \tanh kH}} \quad (2.22)$$

$$c_g = \frac{c}{2} \left[1 + \frac{2kH}{\sinh 2kH} \right] \quad (2.23)$$

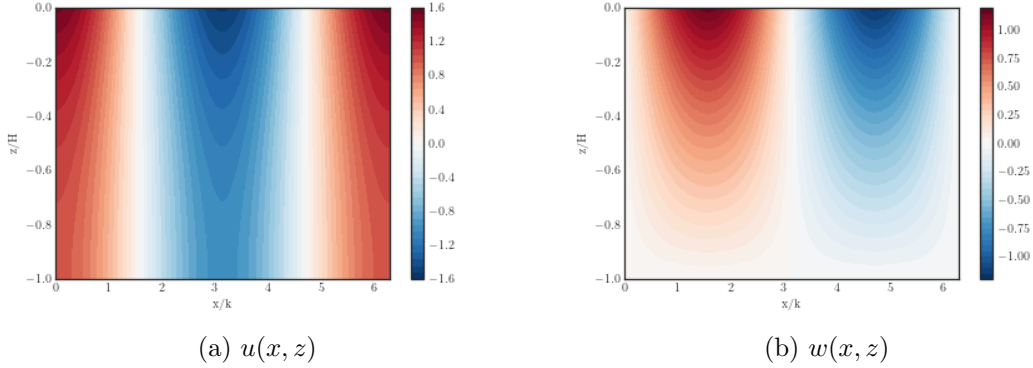


Figure 2.1: Normalized plot of functions $u(x, z)$ and $w(x, z)$ for $t = 0$. The parameter values are $k = 1$ and $H = 1$. The x axis goes all over one period (from $x = 0$ to $x = 2\pi$). Here we can see the typical behaviour of water waves in a basin: we have a maximum of w at $x = \frac{\pi}{2}$ and a minimum in $x = \frac{3}{2}\pi$. Horizontal velocity behaves as the maximum of vertical velocity "attracted" water.

Deep and shallow water approximations

Due to the dispersion relation (2.21) being non-linear, the behaviour of c and c_g is not always clearly visible from (2.22) and (2.23). Often *deep water* and *shallow water* approximations are used to simplify the problem. Deep water approximation occurs when $kH \gg 1$ (i.e. the wavelength of the perturbation is far smaller than depth of the water basin: $\lambda \ll 2\pi H$), so that $\tanh kH \approx 1$ and we obtain

$$c = \sqrt{\frac{g}{H}} \quad (2.24)$$

$$c_g = \frac{c}{2} \quad (2.25)$$

Alternatively, when $kH \ll 1$ (i.e. $\lambda \gg 2\pi H$) we are in the shallow water approximation, and in this case we have that $\tanh kH \approx kH$, leading to

$$c = \sqrt{gH} \quad (2.26)$$

$$c_g = \sqrt{gH} = c \quad (2.27)$$

Thus in shallow water approximation the gravity waves are no longer dispersive. (2.26) suggests that smooth variations of the depth of basin H can lead to refraction phenomena.

As in most wave propagation phenomena, Heidarzadeh and Satake 2015 reports that signal wavelength can directly be linked to source dimension. It is reasonable to assume that if the source characteristic dimension is L , $\lambda = 2L$, where λ is the signal wavelength.

Given (2.26) and the basic wave relation $c = \lambda/T$, with T being the signal period, we can have

$$T = \frac{2L}{\sqrt{gH}} \quad (2.28)$$

2.3 Non-linear shallow water theory

In the particular frame of shallow water waves, that is, when the typical depths of the basin are way smaller than the typical horizontal lengths (as perturbation wavelength for tsunamis), it is possible to develop a non-linear theory that describes the motion of the water.

The lead presented in Stoker 1992 will be followed. Let us consider an homogeneous incompressible inviscid fluid with density ρ in an infinitely large basin. We set a cartesian frame of reference with origin in the unperturbed surface of the fluid, with z direction pointing upwards and x and y directions oriented horizontally. Let u , v , w be, respectively, the x , y , z components of velocity. The Navier-stokes equations (2.8) translate in:

$$\frac{\partial u}{\partial t} + u \frac{\partial u}{\partial x} + v \frac{\partial u}{\partial y} + w \frac{\partial u}{\partial z} = -\frac{1}{\rho} \frac{\partial p}{\partial x} \quad (2.29a)$$

$$\frac{\partial v}{\partial t} + u \frac{\partial v}{\partial x} + v \frac{\partial v}{\partial y} + w \frac{\partial v}{\partial z} = -\frac{1}{\rho} \frac{\partial p}{\partial y} \quad (2.29b)$$

$$\frac{\partial w}{\partial t} + u \frac{\partial w}{\partial x} + v \frac{\partial w}{\partial y} + w \frac{\partial w}{\partial z} = -\frac{1}{\rho} \frac{\partial p}{\partial z} - g \quad (2.29c)$$

where it is assumed that the only body force acting on the system is gravity. The continuity equation for an incompressible fluid (2.2) holds:

$$\frac{\partial u}{\partial x} + \frac{\partial v}{\partial y} + \frac{\partial w}{\partial z} = 0 \quad (2.30)$$

Let $\eta(x, y, t)$ be the perturbation of the fluid surface and let $-h(x, y)$ be the depth of the basin. At the boundaries we have

$$\frac{d\eta}{dt} = w \quad \text{in} \quad z = \eta(x, y, t) \quad (2.31)$$

$$u \frac{\partial h}{\partial x} + v \frac{\partial h}{\partial y} = -w \quad \text{in} \quad z = -h(x, y) \quad (2.32)$$

Equations 2.32 and 2.31 are *cynematical* boundary conditions, and impose the fluid particles not to leave the surface and not to cross the basin floor. A *dynamical* boundary condition on the pressure is also imposed:

$$p = 0 \quad \text{in} \quad z = \eta(x, y, t) \quad (2.33)$$

We integrate (2.30) all over the depth of the basin:

$$\int_{-h(x,y)}^{\eta(x,y)} \left(\frac{\partial u}{\partial x} + \frac{\partial v}{\partial y} \right) dz = - \left[w \right]_{-h(x,y)}^{\eta(x,y,t)} \quad (2.34)$$

Substituting (2.32) and (2.31) in RHS of (2.34) we obtain

$$\int_{-h(x,y)}^{\eta(x,y)} \left(\frac{\partial u}{\partial x} + \frac{\partial v}{\partial y} \right) dz = - \left(\frac{d\eta}{dt} + u|_{-h} \frac{\partial h}{\partial x} + v|_{-h} \frac{\partial h}{\partial y} \right) \quad (2.35)$$

Now considering that

$$\frac{\partial}{\partial x} \int_{-h}^{\eta} u dz = u|_{\eta} \frac{\partial \eta}{\partial x} + u|_{-h} \frac{\partial h}{\partial x} + \int_{-h}^{\eta} \frac{\partial v}{\partial x} dz$$

we find

$$\int_{-h}^{\eta} \frac{\partial v}{\partial x} dz = \frac{\partial}{\partial x} \int_{-h}^{\eta} u dz - u|_{\eta} \frac{\partial \eta}{\partial x} - u|_{-h} \frac{\partial h}{\partial x} \quad (2.36)$$

In the same fashion we can easily find

$$\int_{-h}^{\eta} \frac{\partial v}{\partial y} dz = \frac{\partial}{\partial y} \int_{-h}^{\eta} v dz - v|_{\eta} \frac{\partial \eta}{\partial y} - v|_{-h} \frac{\partial h}{\partial y} \quad (2.37)$$

Inserting (2.36) and (2.37) in (2.35), and considering that

$$\frac{d\eta}{dt} = \frac{\partial \eta}{\partial t} + u|_{\eta} \frac{\partial \eta}{\partial x} + v|_{\eta} \frac{\partial \eta}{\partial y}$$

we obtain

$$\frac{\partial}{\partial x} \int_{-h}^{\eta} u dz + \frac{\partial}{\partial y} \int_{-h}^{\eta} v dz = - \frac{\partial \eta}{\partial t} \quad (2.38)$$

Now we assume that the effect of the vertical acceleration $\frac{dw}{dt}$ upon the pressure p is negligible, that is, the fluid is in hydrostatic configuration, so that

$$p = \rho g(\eta - z) \quad (2.39)$$

So $\frac{\partial p}{\partial x} = g \frac{\partial \eta}{\partial x}$ and from (2.29a) we see that $\frac{du}{dt}$ does not depend on z . Thus, if u doesn't depend on z at any instant t , it is always independent from z , so that

$$\int_{-h}^{\eta} u dz = u(\eta + h)$$

The same holds true for the y component, so we can finally rewrite (2.38) as

$$\frac{\partial (u(\eta + h))}{\partial x} + \frac{\partial (v(\eta + h))}{\partial y} = - \frac{\partial \eta}{\partial t}$$

So, our final system of equations is

$$\frac{\partial u}{\partial t} + u \frac{\partial u}{\partial x} + v \frac{\partial u}{\partial y} = -g \frac{\partial \eta}{\partial x} \quad (2.40a)$$

$$\frac{\partial v}{\partial t} + u \frac{\partial v}{\partial x} + v \frac{\partial v}{\partial y} = -g \frac{\partial \eta}{\partial y} \quad (2.40b)$$

$$\frac{\partial w}{\partial t} + u \frac{\partial w}{\partial x} + v \frac{\partial w}{\partial y} + w \frac{\partial w}{\partial z} = 0 \quad (2.40c)$$

$$\frac{\partial (u(\eta + h))}{\partial x} + \frac{\partial (v(\eta + h))}{\partial y} = -\frac{\partial \eta}{\partial t} \quad (2.40d)$$

Water columns model

Another way to obtain (2.40) is to consider all the quantities to be referring to *mean values* of an entire column of water. This transforms a 3-dimensional problem in a 2-dimensional one, removing every dependency from z from the beginning. This approximation holds as long as the vertical variations have length scales far greater than the basin depth $h(x, y)$, that is, when the shallow water approximation holds firmly. In the particular case of tsunamis, we are usually interested in horizontal propagation of long waves, so in this work (2.40) will be used neglecting (2.40c), whose information is out of our interest.

As shown in Goto et al. 1997 we can define the total height of the water columns $D = \eta + h$ and the *discharge fluxes* M and N :

$$M = uD = u(\eta + h) \quad (2.41a)$$

$$N = vD = v(\eta + h) \quad (2.41b)$$

Integrating eqns. (2.40) between $-h$ and η and using (2.41a) and (2.41b) we can rewrite (2.40) as:

$$\frac{\partial M}{\partial t} + \frac{\partial}{\partial x} \left(\frac{M^2}{D} \right) + \frac{\partial}{\partial y} \left(\frac{MN}{D} \right) + gD \frac{\partial \eta}{\partial x} = 0 \quad (2.42a)$$

$$\frac{\partial N}{\partial t} + \frac{\partial}{\partial x} \left(\frac{MN}{D} \right) + \frac{\partial}{\partial y} \left(\frac{N^2}{D} \right) + gD \frac{\partial \eta}{\partial y} = 0 \quad (2.42b)$$

$$\frac{\partial \eta}{\partial t} + \frac{\partial M}{\partial x} + \frac{\partial N}{\partial y} = 0 \quad (2.42c)$$

Friction between water column and basin floor The only external force present in (2.42) is gravity, but in tsunami propagation problems the friction between the water column and the basin floor f_x and f_y must be accounted for. As seen in Dao and Tkalich

2007, the friction can be expressed by:

$$f_x = \frac{gn^2}{D^{\frac{7}{3}}} M \sqrt{(M^2 + N^2)} \quad (2.43a)$$

$$f_y = \frac{gn^2}{D^{\frac{7}{3}}} N \sqrt{(M^2 + N^2)} \quad (2.43b)$$

where n is the Manning's roughness coefficient. In tsunami propagation problems typical values of n range from $0.01 \text{ m}^{-1/3}\text{s}$ and $0.06 \text{ m}^{-1/3}\text{s}$.

In this way, the final system of equations describing long waves propagating in shallow water, in water column model, is given by:

$$\frac{\partial M}{\partial t} + \frac{\partial}{\partial x} \left(\frac{M^2}{D} \right) + \frac{\partial}{\partial y} \left(\frac{MN}{D} \right) + gD \frac{\partial \eta}{\partial x} + \frac{gn^2}{D^{\frac{7}{3}}} M \sqrt{(M^2 + N^2)} = 0 \quad (2.44a)$$

$$\frac{\partial N}{\partial t} + \frac{\partial}{\partial x} \left(\frac{MN}{D} \right) + \frac{\partial}{\partial y} \left(\frac{N^2}{D} \right) + gD \frac{\partial \eta}{\partial y} + \frac{gn^2}{D^{\frac{7}{3}}} N \sqrt{(M^2 + N^2)} = 0 \quad (2.44b)$$

$$\frac{\partial \eta}{\partial t} + \frac{\partial M}{\partial x} + \frac{\partial N}{\partial y} = 0 \quad (2.44c)$$

(2.44) are heavily non-linear, and analytical solutions can be found only in particular cases (i.e. neglecting the friction terms and with particular initial values or boundary conditions) so a numerical integration is needed.

2.4 Numerical integration for tsunami propagation: the UBO-TSUFDF software

As eqns. (2.44) can only be analytically solved for simpler cases, numerical integration is needed. In order to obtain the results presented in chapter 3, the UBO-TSUFDF software has been used. UBO-TSUFDF, developed and maintained by the Tsunami Research Team of University of Bologna and presented in Tinti and Tonini 2013, uses a finite difference method through the staggered grids technique and a leap-frog numerical scheme. This allows to find numerical solutions for equations (2.44), accounting for tsunami propagation and inundation of dry land. Several other works used UBO-TSUFDF software to provide successful results in tsunami simulation research, such as Gallotti et al. 2021, Zaniboni et al. 2021 and Triantafyllou et al. 2020 among others. In this section, only the main characteristics of the software will be presented. See Tinti and Tonini 2013 for more informations.

Computational domain UBO-TSUFDF uses a staggered grids numerical scheme, that consists in the superimposition of two rectangular grids with spacings Δx and Δy , one

shifted half a step with respect to the other, in order to have points with integer coordinates $x_i, y_j = (i\Delta x, j\Delta y)$ and points with half-integer coordinates $(x_{i+1/2}, y_{j+1/2}) = ((i + 1/2)\Delta x, (j + 1/2)\Delta y)$. A water depth value h_{ij} is associated to each point of the of the whole grid.

To each point is associated a water depth $h_{i,j}$. $h_{i,j}$ is taken positive for submerged points and negative for emerged points. Even the time domain is discretized in half-steps, so that instant $t_k = k\Delta t$ and instant $t_{k+1/2} = (k + 1/2)\Delta t$.

Numerical scheme UBO-TSUFDF uses a leapfrog scheme to integrate eqns. (2.44). Water elevation η is calculated only in the integer coordinates and discharge fluxes M and N are calculated only in half-integer coordinates. Detailed information about the numerical scheme are found in Tinti and Tonini 2013, while more information can be found in Goto et al. 1997.

In order for the leapfrog scheme to be stable, Von Neumann stability criterion requires $\min(\Delta x, \Delta y) > c_{\max}\Delta t$, where c_{\max} is the maximal phase velocity of the tsunami wave. As $c_{\max} = \sqrt{g \max(h + \eta)}$, the actual allowed value of c_{\max} depend directly upon integration results via η . Small wave approximation (i.e. $h \gg \eta$) is often adopted, so the upper limit for the time step Δt can be determined from the spatial steps Δx and Δy and the maximum water depth in the computational domain h_{\max} .

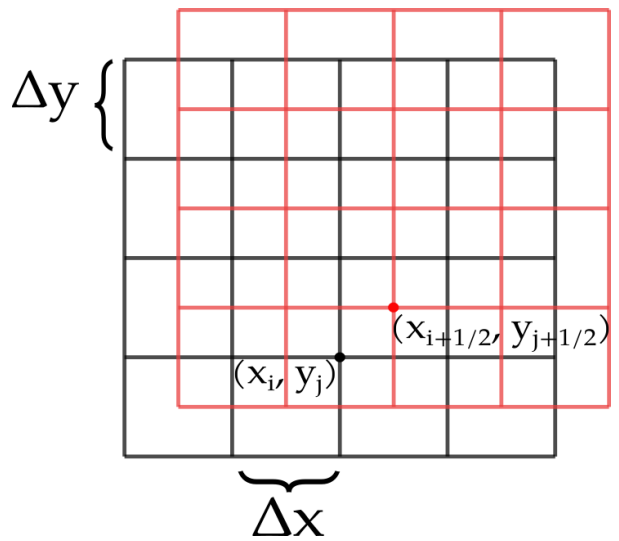


Figure 2.2: Example of staggered grid domain. The black grid represents the integer-indexed grid, while the red one represents the half-integer-indexed one. The nodes of each grid are the actual point in which functions are calculated.

Boundary conditions UBO-TSUFDF supports both free transmission and full reflectivity boundary conditions. The former consists in letting the signal travel outside the computational domain, and is thus used when the boundary represents an open water border. The latter consists in making the signal reflect towards the oncoming direction as if the boundary represents a vertical wall, thus being useful when simulating tsunami propagation in closed basins. It should be pointed out that the staggered grids computational domain causes boundary asymmetries to arise. This is taken into account in the determination of boundary conditions.

Input condition UBO-TSUFDF supports two kind of input condition to start the signal propagation. The former is input via an initial condition: the user inputs an initial perturbation in a particular subset of the grid, and the software propagates the signal. This is used when the tsunami source is within the integration domain. The latter is via boundary conditions: a non-zero signal is given in a subset of the boundary and then propagated. This is used when the tsunami source is outside the integration domain and the user is interested in finding how the external signal propagates within the domain. In addition, input condition can be chosen to be seismic (i.e. and instantaneous perturbation) or non-seismic (i.e. the input signal has a finite duration and can change in time).

Run-up UBO-TSUFDF is able to model the run-up of waves onto dry land. An instantaneous shoreline is identified at each timestep. A threshold water column depth D_{TH} is attached to each cell. If $D > D_{TH}$ the cell is considered to be wet, otherwise the cell is considered dry. Further control on a cell is made by considering the wet/dry status of adjacent cells (in both x and y direction), in order to prevent results to be affected by noise: if a shoreline cell (i, j) is found wet but adjacent cells $(i - 1, j)$ and $(i + 1, j)$ are found to be dry, then cell (i, j) is set as dry. The discharge flux between two adjacent dry cells is set as 0, regardless of previously calculated values. Moreover, if cell (i, j) is found to be dry and cells $(i + 1, j)$ and $(i + 2, j)$ are found to be wet, the boundary between cell (i, j) and $(i + 1, j)$ is considered the instantaneous shoreline, and at this boundary the water velocity value is set equal to the one between cells $(i + 1, j)$ and $(i + 2, j)$, so that the discharge flux $M_{i+1/2,j}^{k+1/2}$ is set as

$$M_{i+1/2,j}^{k+1/2} = M_{i+3/2,j}^{k+1/2} \frac{D_{i+1,j}^k}{D_{i+1,j}^k - D_{i+2,j}^k} \quad (2.45)$$

The same is done along y direction.

Chapter 3

Case study and numerical setup

The aim of this work is to test different kinds of sources in order to numerically recreate the recorded calving tsunami wave. This work is intended to continue the study proposed in Zaniboni et al. 2018. In sect. 3.1 the case study used in this work will be presented, describing the event and analyzing the data. Sect. 3.2 will describe how the integration domain has been selected. Sect. 3.3 will present the sources that have been tested in this work.

3.1 Case study: the August 21st 2009 calving tsunami in Jakobshavn Isbræ

The case study consists in a calving tsunami event observed on August 21st 2009 in Jakobshavn Isbræ.

Jakobshavn Isbræ (Sermeq Kujalleq in Greenlandic) is one of the largest outlet glacier in Western Greenland, near the village of Ilulissat (see fig. 3.2). The Ilulissat fjord, that hosts the glacier, has been declared UNESCO World Heritage Site in 2004 (UNESCO 2021). The glacier and its fjord have been object of study for different works, e.g. Amundson et al. 2012, Walter et al. 2013, Sergeant et al. 2016 among others, for its importance, as it drains a good portion (Echelmeyer et al. 1991 reports 6.5%, more recent estimates as Motyka et al. 2011 report 5.4%) of Greenland Ice Sheet and hosts several calving events in the warm seasons. Climate warming has caused the glacier to thin and retreat since the beginning of the 2000s, causing an increase of its calving rate (Luckman and Murray 2005, Joughin et al. 2008b).

On August 21st 2009 a calving event has been observed and reported by Walter et al. 2012 (a time-lapse footage of the event can be seen in the supplementary material of the paper). The grounded terminus of the glacier detached and created a 700-1000 m long and 500 m wide iceberg, that capsized with a bottom-out rotation. Walter et al. 2012 reports the event began at 06:56:31 UTC and lasted around 5 minutes. A smaller event



Figure 3.1: Satellitar image of Greenland. The red rectangle shows the position of Jakobshavn Isbræ. Image taken and modified from Google Earth (<https://earth.google.com>).



Figure 3.2: Satellitar image of Jakobshavn Isbræ. The positions of ILULI tide gauge, in the harbor of Ilulissat town (purple), and WIND temporary seismic station, next to Tissarissq bay (green) are shown. Red rectangle shows the approximate location of KANGIA tide gauge. Image taken and modified from Google Earth (<https://earth.google.com>).

followed at 07:04:31 UTC, consisting in the top-out rotation from the terminus. Walter et al. 2012 reports that this iceberg was about 3 times smaller in volume and that the capsizing lasted about 3 minutes. The total calved volume is estimated to be around 0.5 km^3 .

Data and preprocessing

Two tide gauges have recorded sea levels oscillations before and after the calving event. ILULI, permanent, is located inside the harbor of Ilulissat, close to the seamount of Ilulissat Icefjord. KANGIA, temporary, was located in Tissarissaq bay, about 6 km West of WIND seismic station. Its precise location is unknown. Position of ILULI tide gauge and WIND seismic station are shown in fig. 3.2. The considered KANGIA data were recorded from August 15th 2009 to August 24th 2009 taking one sample every 30s (sampling frequency $\sim 0.0333 \text{ Hz}$), while the ILULI data were recorded from August 8th 2009 to August 30th 2009 taking one sample every 60s (sampling frequency $\sim 0.016 \text{ Hz}$). Both stations measured water pressure in hPa. Raw data for both records are shown in fig. 3.3.

In order to compare these data with the results produced by UBO-TSUFDF, its pressure data P_i (measured in hPa) are converted into water perturbation η_i (measured in m) via the relation $\eta_i = 100(P_i - P_0)/\rho g$, where $\rho = 1000 \text{ kg m}^{-3}$ is the water density, $g = 9.81 \text{ m s}^{-2}$ is the gravitational acceleration and P_0 is the mean measured pressure value. Converted data can be seen in fig. 3.4.

Also, spectral analysis has been performed on both datasets to obtain the power spectral density (PSD) of the signal. Results are shown in fig. 3.5. From PSD is easy to distinguish to main peaks at very long periods ($\sim 10^5 \text{ s}$) in both KANGIA and ILULI record, probably due to the 12 and 24 hours tide cycles. Other high period local maxima, more distinguishable in KANGIA, are probably due to seiches.

In order to remove these long-period interfering signals from the data, an high-pass filter has been applied to both dataset using a cut-off frequency $\nu_{cut} = 1/14000 \text{ Hz}$ (i.e. $14000 \text{ s} = 4 \text{ hrs}$ cut-off period). Filtered data are represented in fig. 3.6.

From these, it is easier to recognize the August 21st and 22nd tsunamis in both datasets. The peak amplitudes in KANGIA are roughly one order of magnitude greater. Overall, ILULI seems to host more impulsive signals than KANGIA. Figs 3.7 and 3.8 show the filtered signal produced by the tsunami. In KANGIA the first wave peak is more than 1 m high, followed by some smaller amplitude waves. The signal detected in ILULI shows larger periods, and the wave seems to arrive $\sim 5 \text{ min}$ later than KANGIA. Spectral analysis on the 10 hours window of tsunami signal has also been performed. For comparison, the same has been done for the background signal, using 10 hours of data that did not present any sign of impulsive events. Results can be seen in fig.s 3.9 for ILULI and 3.10 for KANGIA.

From these, we can see that some peaks, e.g. the $\sim 200 \text{ s} \simeq 3 \text{ min}$ peak in ILULI,

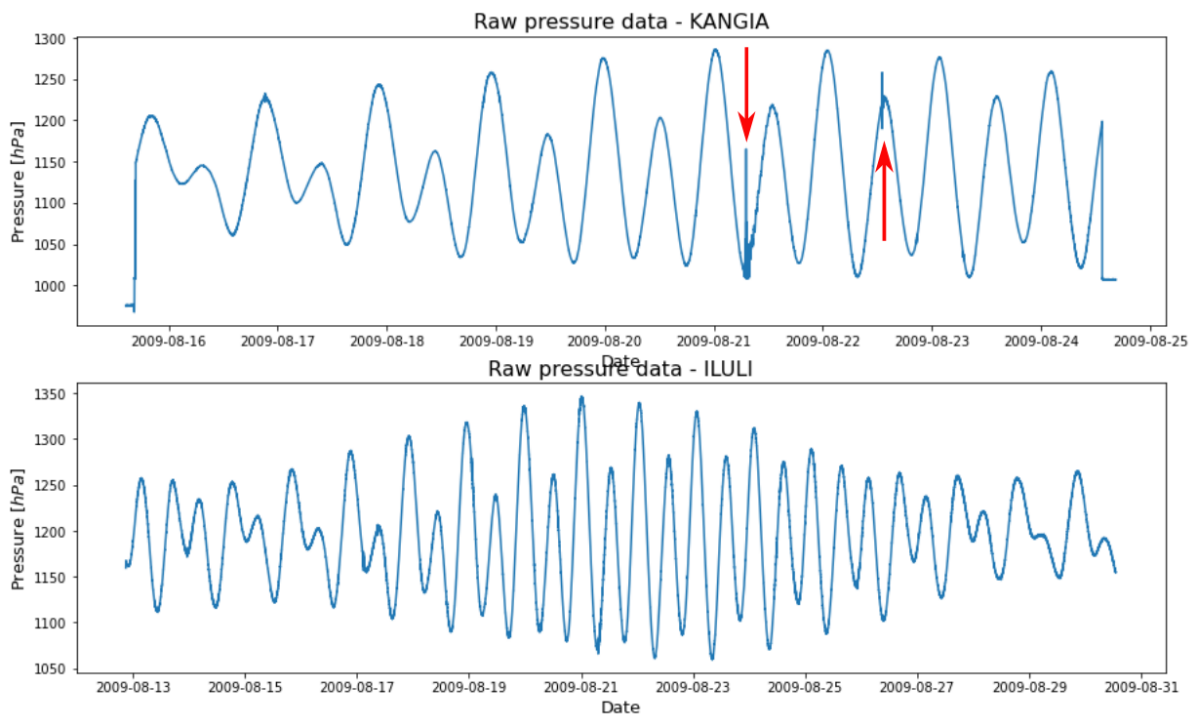


Figure 3.3: Raw data from KANGIA and ILULI tide gauges. In both marigrams, main variations are due to tides. In KANGIA data it is possible to recognize the 21/08 tsunami signal. It is also possible to see the signal of another smaller tsunami happened in 22/08. These events are marked with the red arrows.

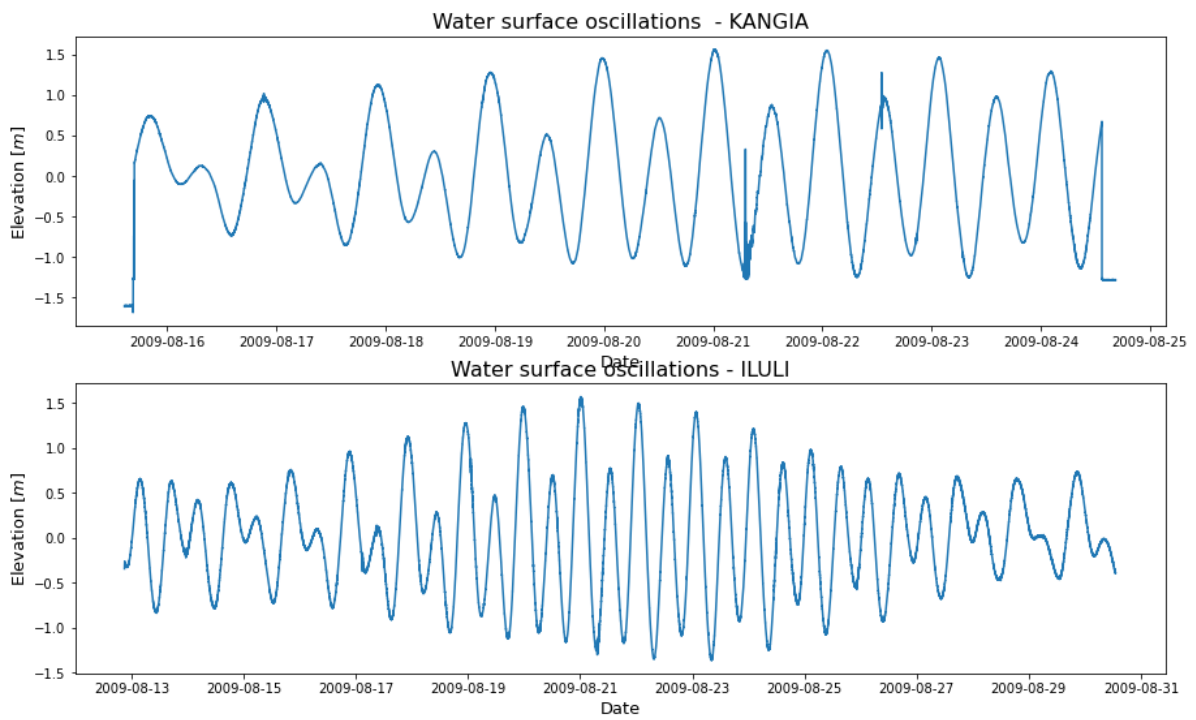


Figure 3.4: Water perturbation obtained from KANGIA and ILULI datasets after conversion.

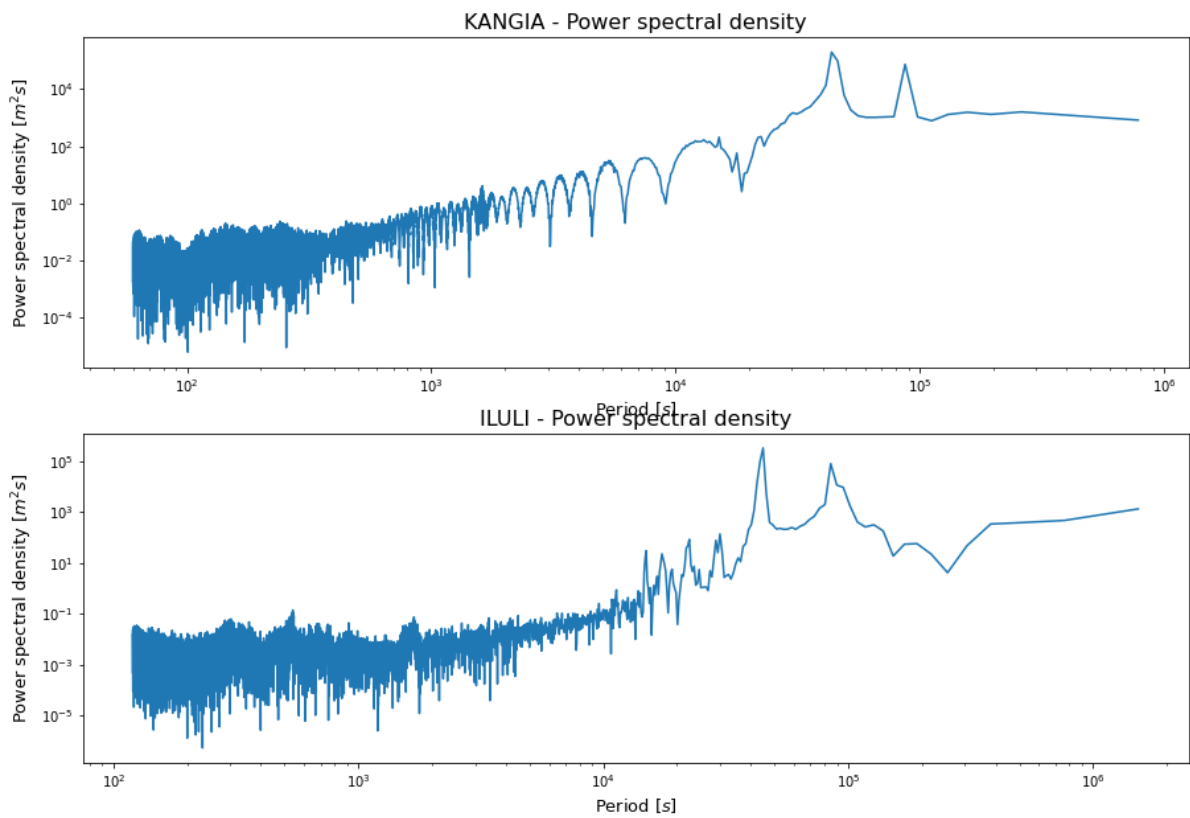


Figure 3.5: Power spectral density (PSD) for the processed data for both ILULI and KANGIA datasets.

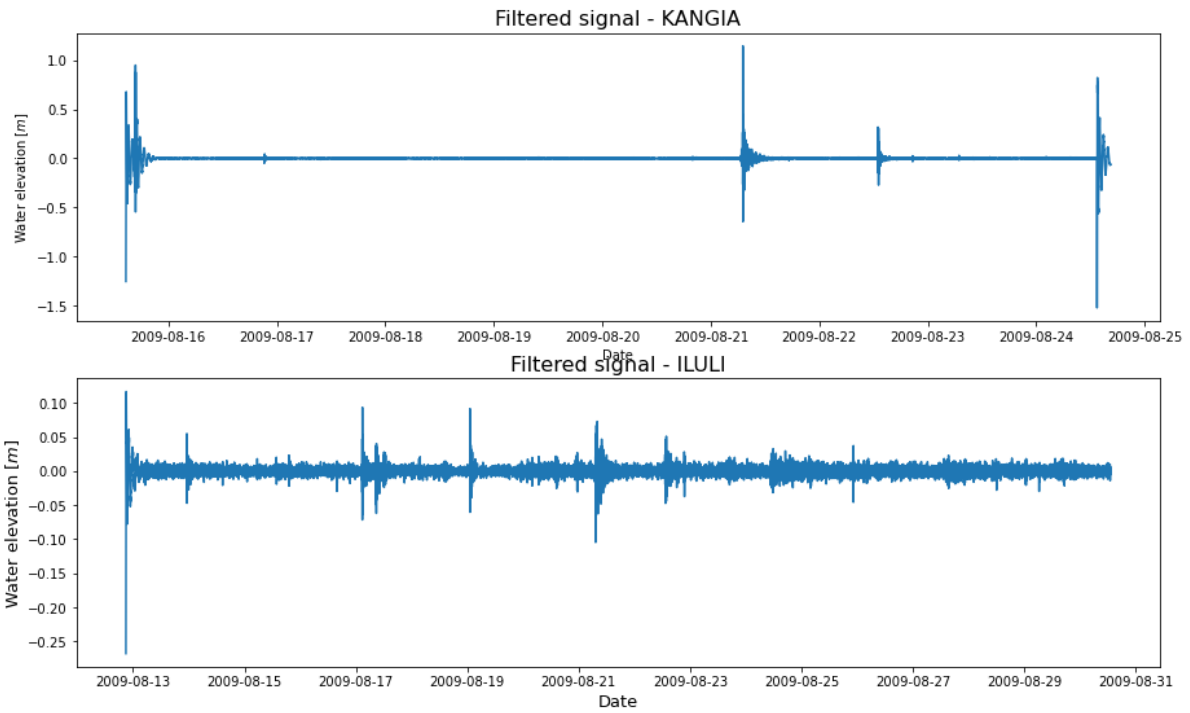


Figure 3.6: Filtered signal for KANGIA and ILULI. Note that the y -scales are different between the two images.

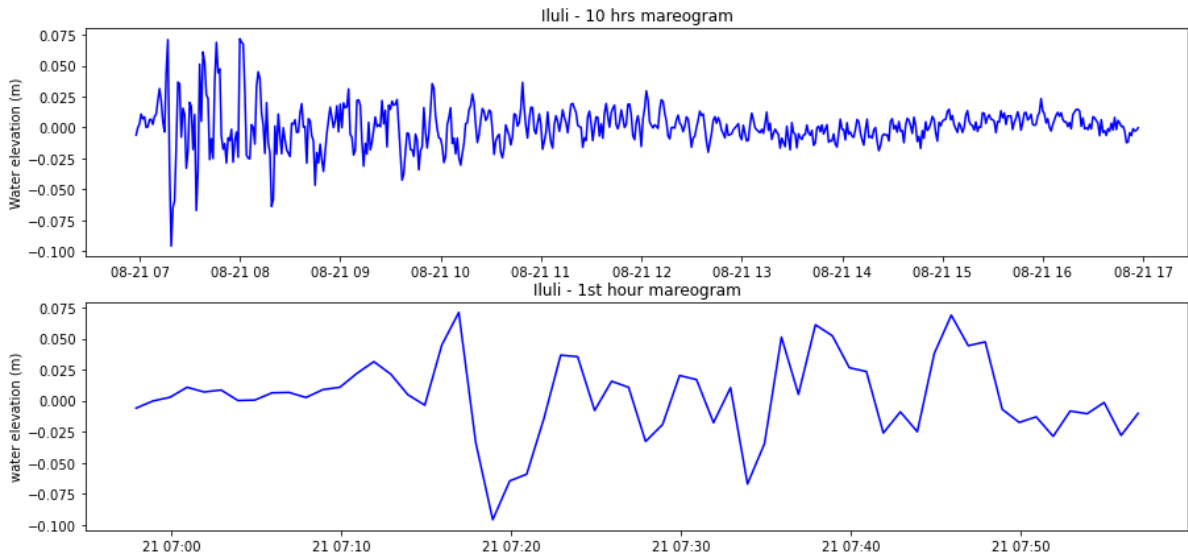


Figure 3.7: Signal produced by the calving event in ILULI station. Top: 10 hours signal, showing the event and the wave train. Bottom: zoom on the event and the following hour of signal.

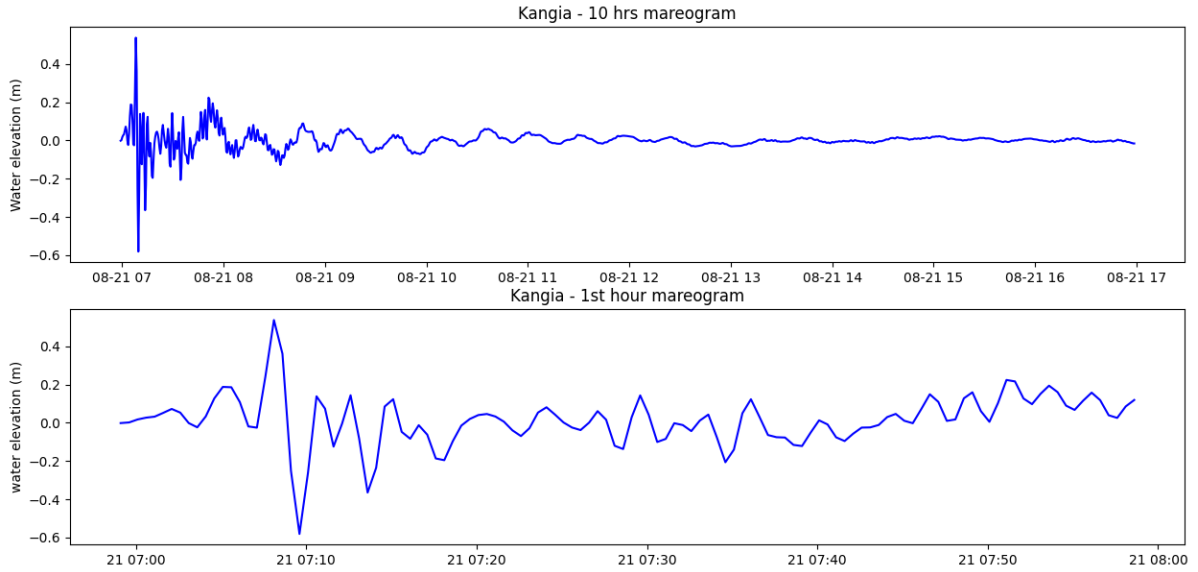
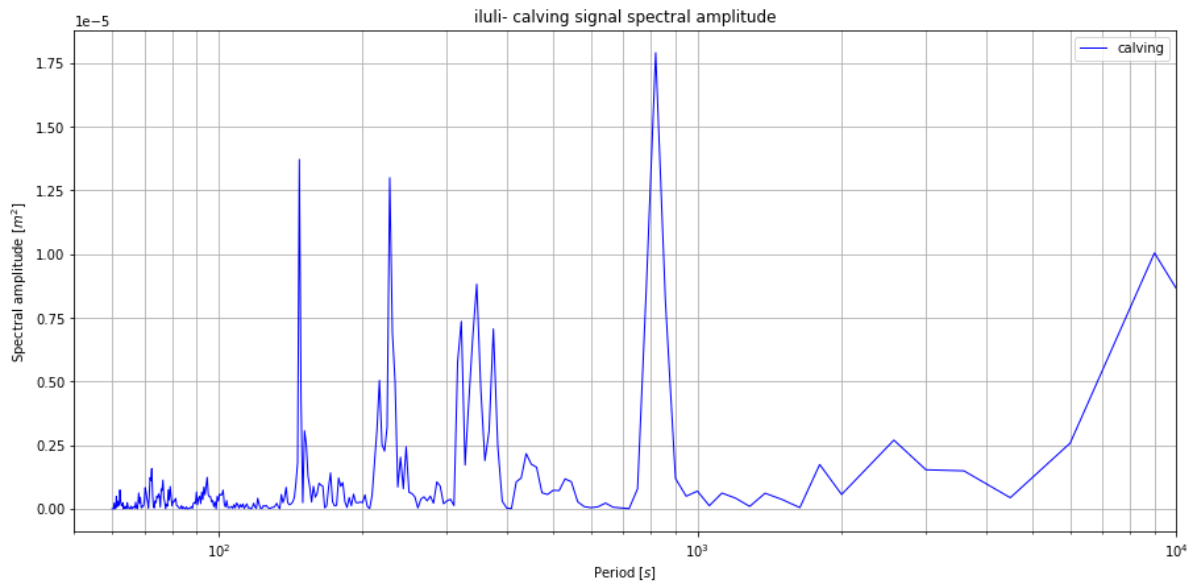


Figure 3.8: Signal produced by the calving event in Kangia station. Top: 10 hours signal, showing the event and the wave train. Bottom: zoom on the event and the following hour of signal.

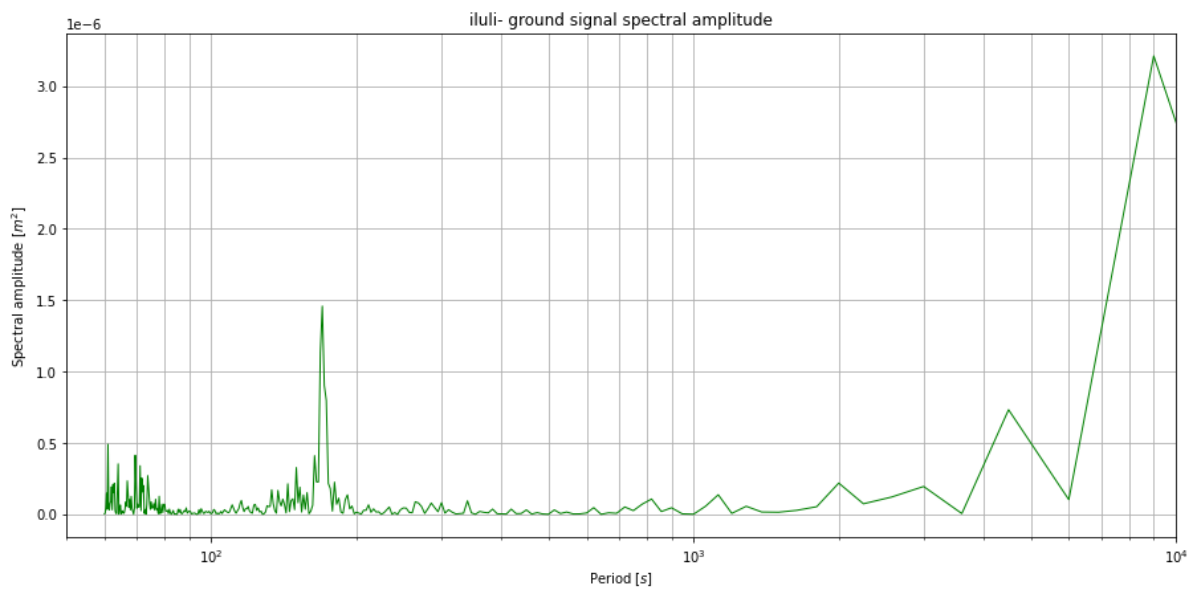
the $\sim 1500 - 1600\text{ s} \simeq 25\text{ min}$ for KANGIA and the $\sim 10^4\text{ s} \simeq 3\text{ hrs}$ for both datasets are present in both the background and tsunami-perturbed signals. These signals are probably due to the Ilulissat harbor (for ILULI) and Jakobshavn fjord (for KANGIA) seiches. The 25 min signal in KANGIA is highly amplified in the perturbed signal, suggesting that the tsunami has excited a resonance. The same holds true for the 180 s signal in ILULI, that is present in both the perturbed and unperturbed signal. The greatest peak at 25 min is only present in the perturbed signal, and coincides with the main peak recorded in KANGIA, suggesting that this frequency is directly brought by the perturbation from within the fjord. This may also explain the $\sim 200\text{ s}$ peak in the ILULI perturbed signal, as the perturbed KANGIA signal shows small amplitude peaks along those frequencies. The group of peaks within the 300-400s interval cannot be explained in this way, as in KANGIA these components have almost null amplitude. The 3 hours signal, present in both marigrams, may be due to a longitudinal oscillation mode of the fjord, but other causes can also be valid. Moreover, the tsunami adds shorter peak frequencies in the signal, specially in ILULI.

3.2 Simulation setup

The results obtained by the application of the UBO-TSUFDF code strongly depend upon the input integration domain grid. The original dataset has been taken from BedMa-

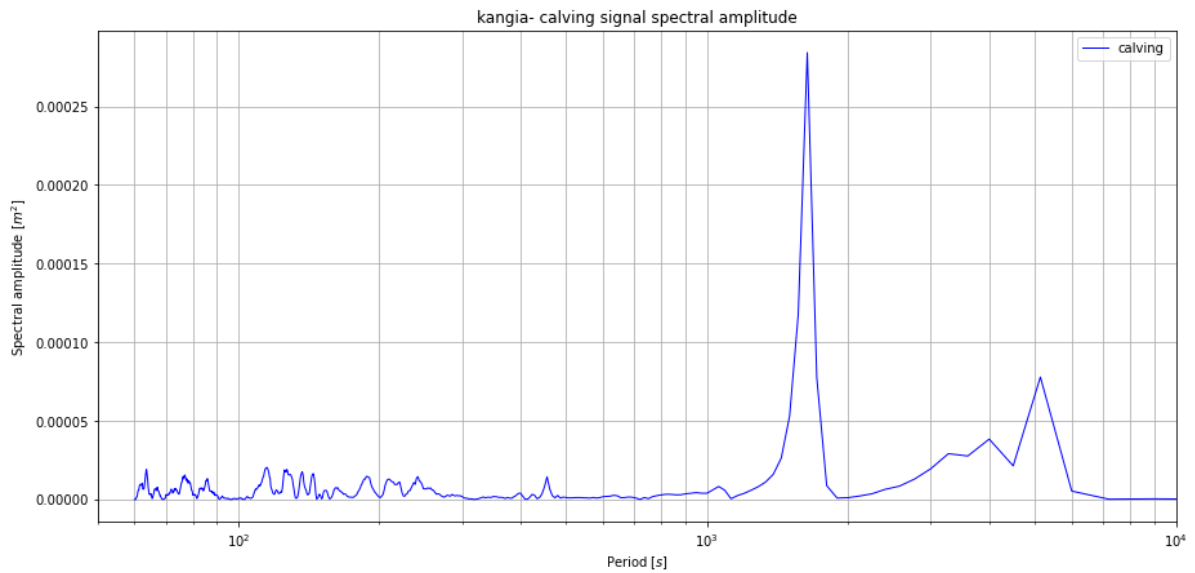


(a) *ILULI - Spectral amplitude of the tsunami wave with a 10 hour window.*

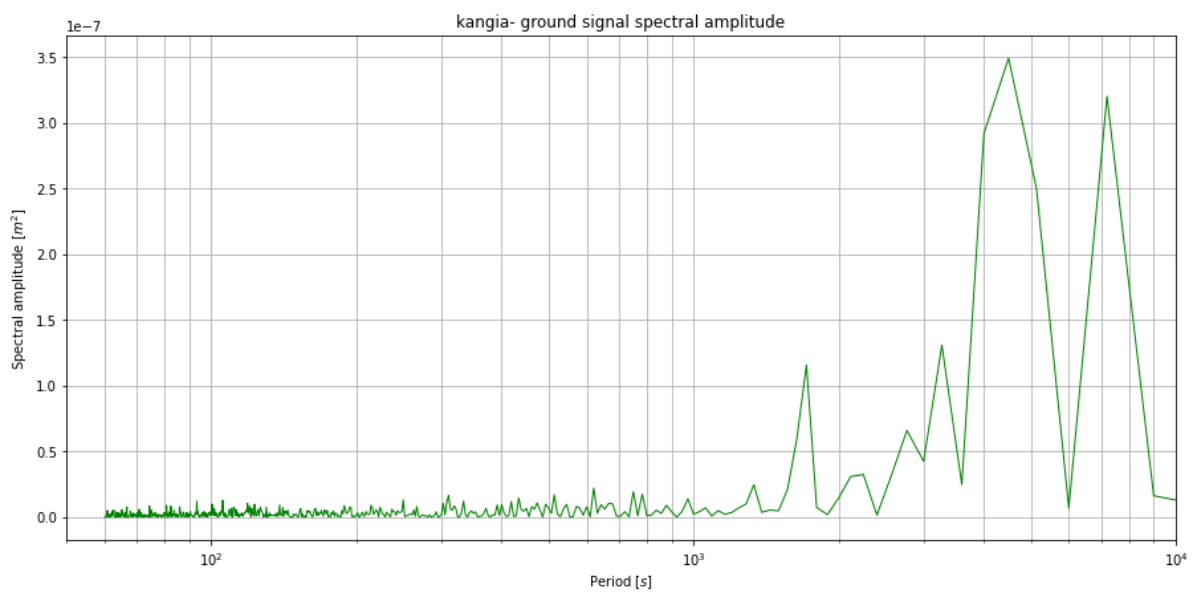


(b) *ILULI - Spectral amplitude of the ground signal with a 10 hours window.*

Figure 3.9: Spectral amplitudes for ILULI dataset, for (a) the calving signal and (b) the ground signal. Note that the vertical axis have different scales.



(a) *KANGIA - Spectral amplitude of the tsunami wave with a 10 hour window.*



(b) *KANGIA - Spectral amplitude of the ground signal with a 10 hours window.*

Figure 3.10: Spectral amplitudes for KANGIA dataset, for (a) the calving signal and (b) the ground signal. Note that the vertical axis have different scales.

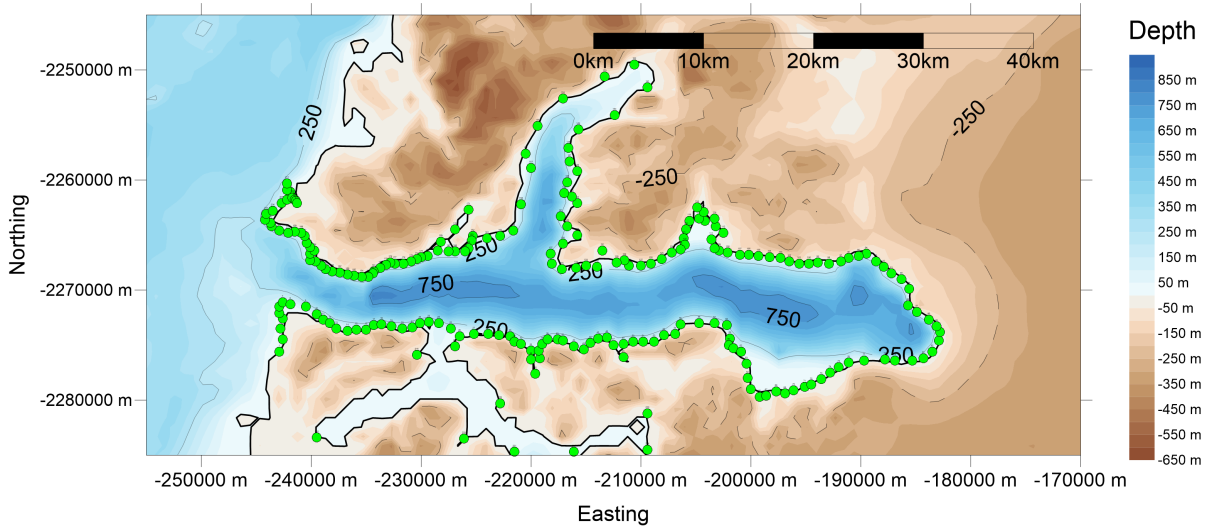
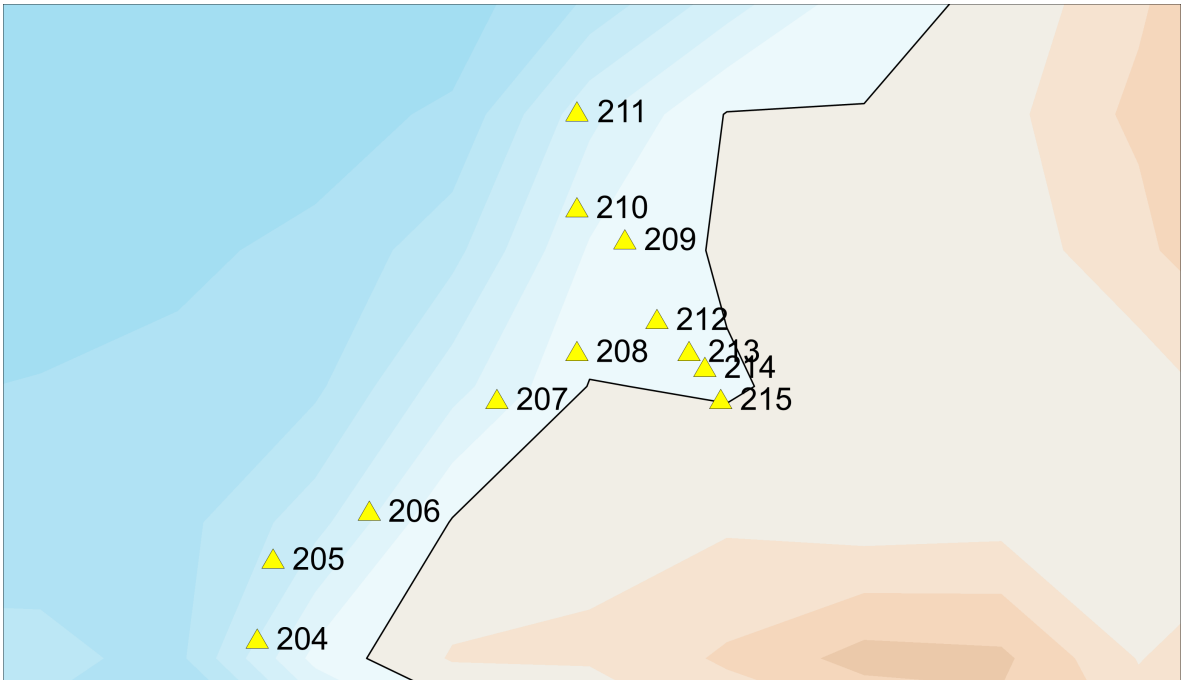
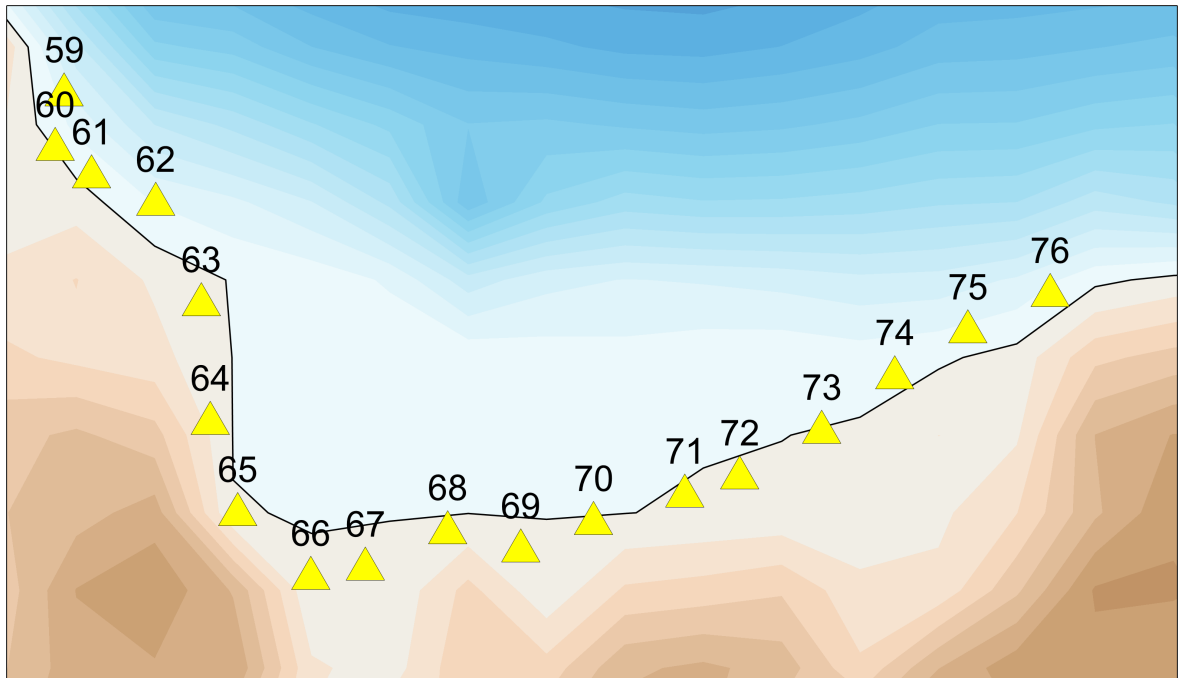


Figure 3.11: Contour-line representation of the integration grid. Level values refer to water depth, so land points have a negative values. The thicker black line represents the shoreline. Green dots mark the position of the virtual mareographs. The red rectangle is the position in which tsunami sources will be positioned. Coordinate reference system is WGS 84/NSIDC Sea Ice Polar Stereographic North with EPSG:3413 projection.

chine Greenland Dataset (*BedMachine Greenland v3*) and has been interpolated into a regularly-spaced mesh. Some adjustments have been done on the grid, in order to reconstruct a shoreline as closer as possible to the one of August 21st 2009, given that the glacier tongue position has great variations across the year, not accounted for in the original data. The resolution in both x and y directions is 100 m. The integration grid that has been used is represented in 3.11. Notice the considerable water depth (more than 800 m) reached in the central portion of the fjord, and the two secondary shallow-water inlets that are not expected to particularly influence the tsunami propagation in the main basin. Virtual tide gauges have been placed all along the shoreline to “record” the simulated signal (see green dots in fig. 3.11). In particular, some of them have been placed in the proximity of the real ones. For ILULI (see fig. 3.12a) marigrams 213, 214 and 215 are within the harbor, but these are placed in a line of single wet points within dry points, so signal propagation will be hindered and numerical noise is expected to grow. For KANGIA (see fig. 3.12b) virtual tide gauges from 69 to 72 are expected to be close to the position of the real tide gauge.



(a) Virtual tide gauges placed close to the actual position of ILULI tide gauge, within the harbor of Ilulissat.



(b) Virtual tide gauges placed along the shoreline of Tissarissoq bay.

Figure 3.12: Positions of the virtual tide gauges in the proximity of the real ones.

3.3 Tested sources

The modeling of the calving mechanism and of the ensuing tsunami wave is particularly complex. Due to the lack of a proper approach to assess the tsunamigenic impulse related to the collapse of ice mass into water, a different strategy has been pursued, computing synthetic initial conditions for the tsunami. In order to investigate the calving-tsunami source, the footage of the event has been analyzed. The first important impulse that seems to form has positive amplitude and is straightforward to assume its dimension is strictly related to the calving event scale. Three different types of source have been investigated and tested: the Asymmetric Single Gaussian (ASG), the Symmetric Double Gaussian (SDG) and the Asymmetric Double Gaussian (ADG). Each source depends on a certain number of parameters, and different combinations have been tested during the investigation.

Asymmetric Single Gaussian (ASG) The source is defined by the function

$$ASG(x, y) = a \exp \left(-\frac{1}{2} \left(\frac{x^2}{\sigma_x^2} + \frac{y^2}{\sigma_y^2} \right) \right) \quad (3.1)$$

and thus depends upon three parameters a , σ_x and σ_y . This source is intended to model the first positive amplitude impulse, and has been designed considering the transversal dimension to be bigger than the longitudinal one (with respect to the tsunami propagation direction). This is intended to reproduce the width of the calving iceberg. A representation of this function can be seen in fig 3.13.

Symmetric Double Gaussian (SDG) The source is defined by the function

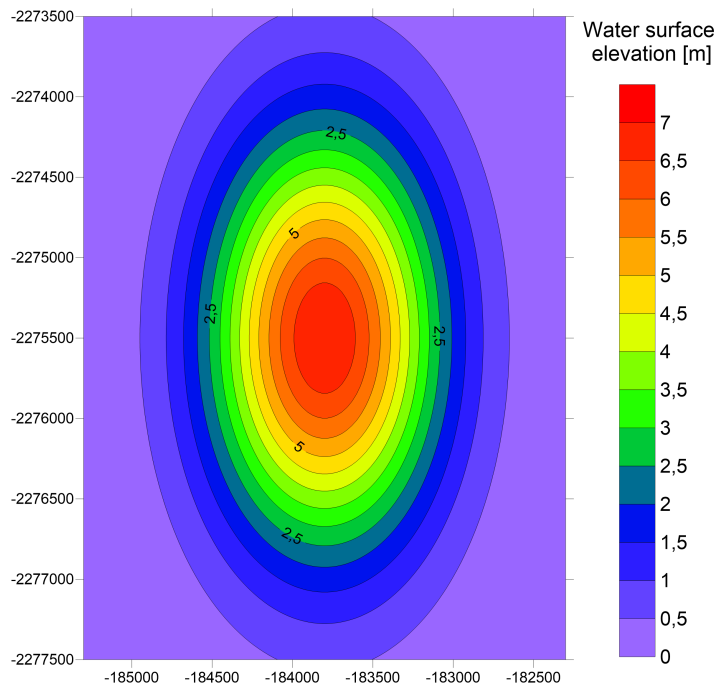
$$SDG(x, y) = a \left(\exp \left(-\frac{(x + \mu)^2 + (y - \mu)^2}{2\sigma^2} \right) - \exp \left(-\frac{(x - \mu)^2 + (y + \mu)^2}{2\sigma^2} \right) \right) \quad (3.2)$$

and thus depends upon three parameters a , μ and σ . This source is meant to reproduce the movement of the iceberg capsizing, up-lifting water in one direction and pushing down water in the opposite one. A representation of this function can be seen in fig 3.14.

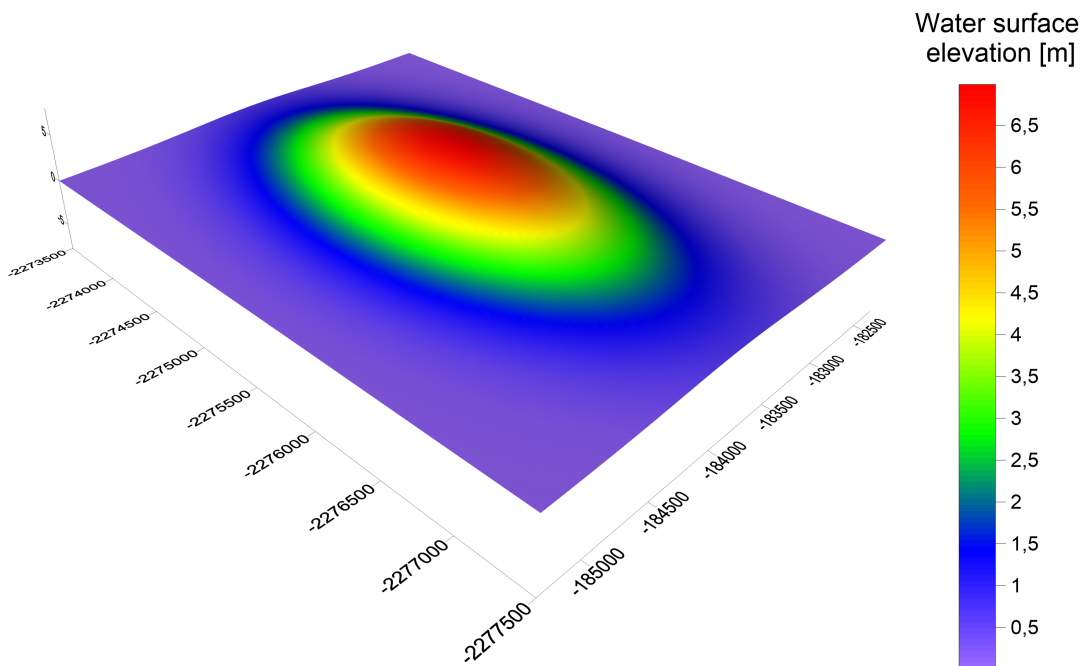
Asymmetric Double Gaussian (ADG) The source is defined by the function

$$ADG(x, y) = a \left(\exp \left(-\frac{(x + \mu)^2}{2\sigma_x^2} - \frac{(y - \mu)^2}{2\sigma_y^2} \right) - \exp \left(-\frac{(x - \mu)^2}{2\sigma_x^2} - \frac{(y + \mu)^2}{2\sigma_y^2} \right) \right) \quad (3.3)$$

and depends upon four parameters: a , σ_x , σ_y and μ , one more than ASG and SDG. This is a sort of summary of the other two sources, trying to account for capsizing movement and iceberg dimensions. A representation of this function can be seen in fig 3.15.

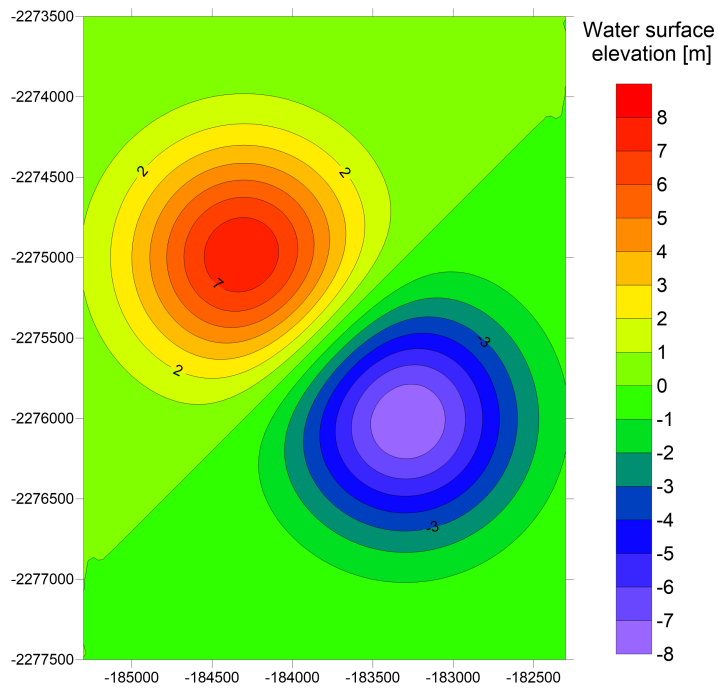


(a) ASG - heightmap plot.

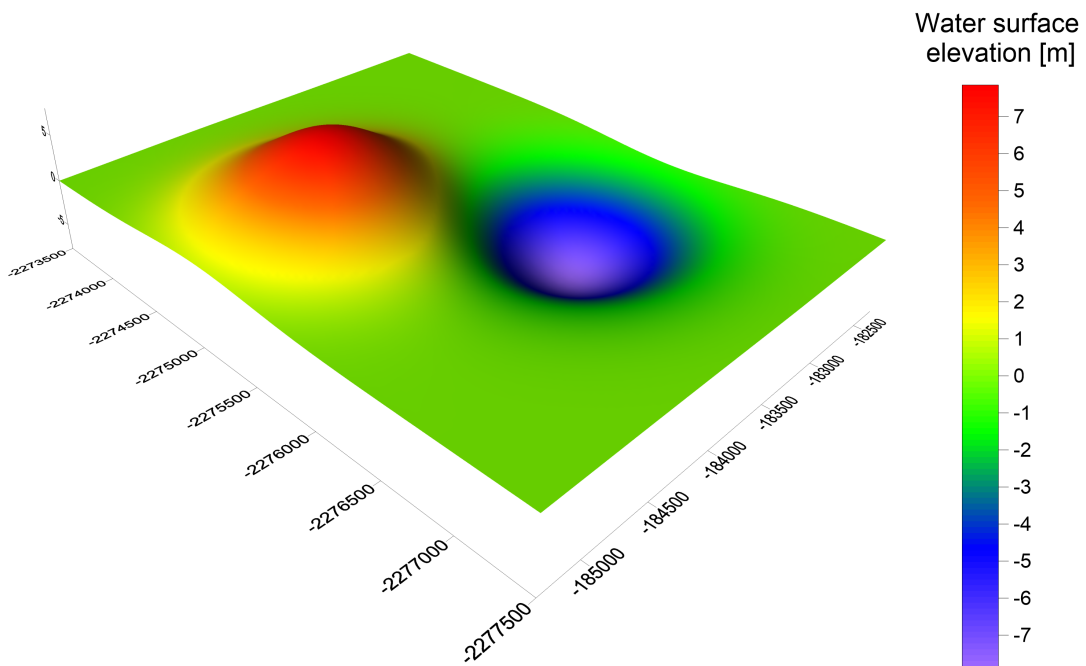


(b) ASG - 3-dimensional surface plot.

Figure 3.13: Plots showing an example of Asymmetric Single Gaussian (ASG) source with parameter values $a = 7$, $\sigma_x = 5$, $\sigma_y = 9$.

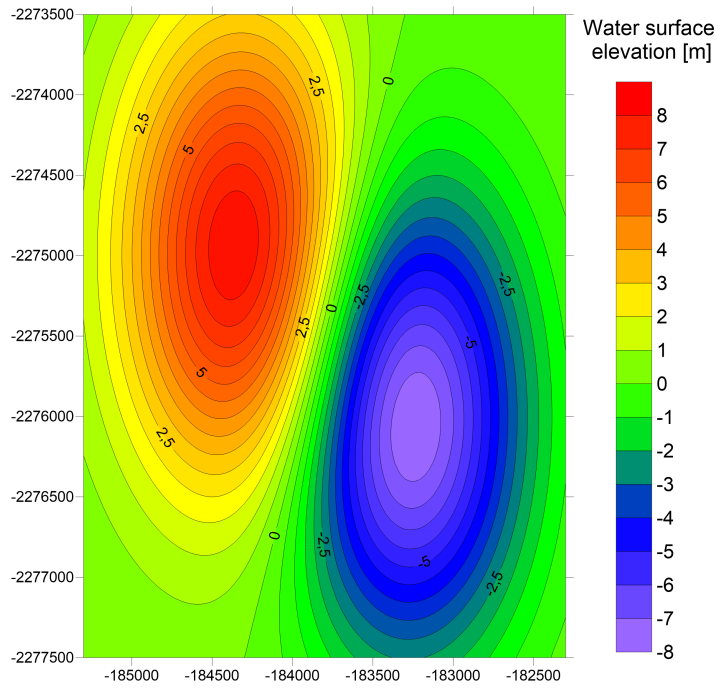


(a) *SDG - heightmap plot.*

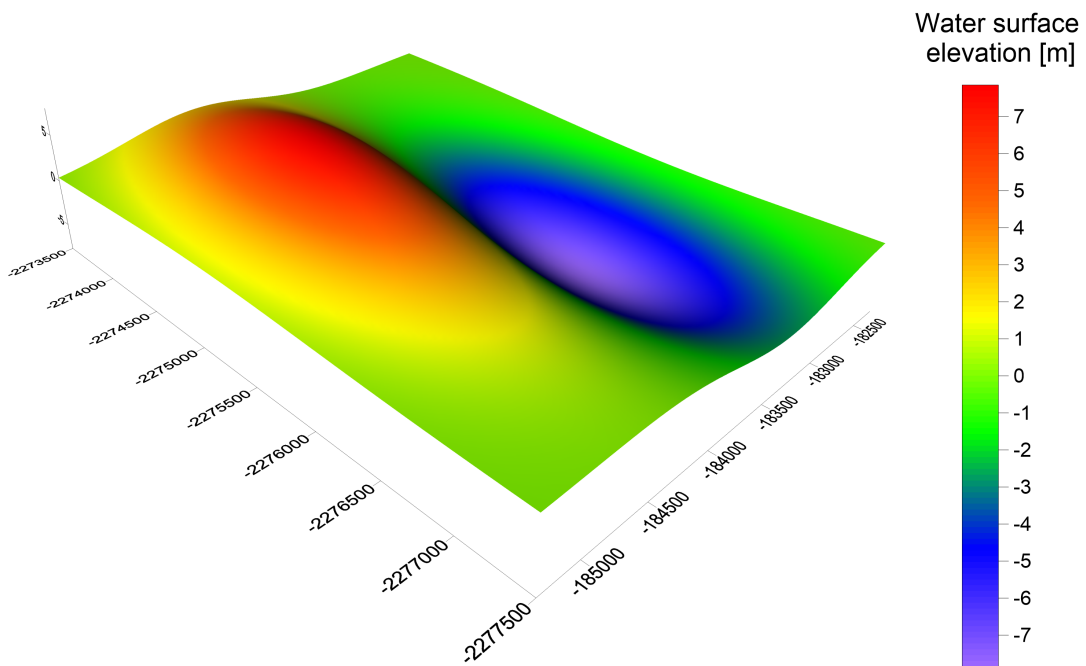


(b) *SDG - 3-dimensional surface plot.*

Figure 3.14: Plots showing an example of Symmetric Double Gaussian (SDG) source with parameter values $a = 8$, $\mu_x = 5$, $\sigma = 5$.



(a) ADG - heightmap plot.



(b) ADG - 3-dimensional surface plot.

Figure 3.15: Plots showing an example of Asymmetric Double Gaussian (ADG) source with parameter values $a = 8$, $\sigma_x = 5$, $\sigma_y = 10$, $\mu = 5$.

In order to obtain a starting condition from these sources, functions are first calculated in a Cartesian grid defined by integer coordinates $X \in [-15, 15]$, $Y \in [-20, 20]$, then each point is translated into the real grid using the transformation

$$\begin{aligned}x &= 100X - 183800 \\y &= 100Y - 2275500\end{aligned}$$

where x, y are the coordinates in the integration domain. In this way the sources are centered right in the position of the calving event.

Chapter 4

Results and discussion

The sources presented in 3.3 have been tested with different parameter values to inspect how well the simulated signal would fit the real one. Confrontation has been carried for both the time signal and the spectral amplitude.

KANGIA The KANGIA record has been compared with the results of the virtual marigrams from 69 to 72. Given that the actual position of the real tide gauge is unknown, a second-wise synchronicity of the arrival times is not as meaningful as in other situations. Result evaluation has therefore focused more on the fitness of the first signal in amplitude, form and period and on the spectral amplitude.

ILULI The ILULI record has been compared with the results of the virtual marigram 212. The real position of ILULI is closer to virtual marigrams 213, 214 and 215, but the wave signal in those is not expected to propagate well (see 3.2). So, marigram 212 (close to the seamouth of the Ilulissat harbor) has been selected as comparison. This marigram has been used as “second order” criterion for judging the quality of the signal, as the recorded tsunami wave is roughly one order of magnitude smaller than the one arrived in KANGIA, and thus more likely to be masked by other signals.

Other uncertainties also play a role in the judgment of the quality of the fit. The low sampling frequency of both the tide gauges (one point per 30 s for KANGIA, one point per 60 s for ILULI) could have caused aliasing of shorter-period signals (e.g. wind waves or anthropic noise), thus creating fake longer-period components. Also, the shoreline in the proximity of the calving zone is reconstructed, so divergences from the true signal could happen. The most significant simulation results will be presented in next section.

4.1 Best results

Here the best result obtained for each source function will be presented and discussed. Each of these will be referred to in the format “ $SRC(p_1, p_2, p_3, p_4)$ ” where “SRC” is the source acronym (i.e. ASG for Asymmetric Single Gaussian, SDG for Symmetric Double Gaussian, ADG for Asymmetric Double Gaussian) and “ (p_1, p_2, p_3, p_4) ” are the values of the four (or three) parameters (i.e. a, σ_x, σ_y for ASG; a, σ, μ for SDG; $a, \sigma_x, \sigma_y, \mu$ for ADG).

ASG(7,5,9) See fig.s 4.1, 4.2, 4.3, 4.4. This source fails to reproduce well the shape of the first impulse in KANGIA. The amplitude of the greatest positive peak is lightly overestimated in virtual marigram 69, while it is heavily overestimated in marigrams 70 and 71. The greatest negative peak is underestimated (in absolute value) in marigrams 69 and 70, while it is completely absent in marigram 71. The virtual marigram 72 doesn’t fit the signal in both amplitude and waveform. The wavelength of the first signal is almost doubled in every considered marigram. The virtual marigram 212 recorded a signal with a period that is roughly half of the duration of ILULI record. The ILULI power spectrum is extremely unfit. Concerning KANGIA, all of the considered virtual marigrams behave in a similar way. The two main peaks in the original data (one around the 2000 s \simeq 25 – 30 min, the other around the 6000 s \simeq 1.5 h) are acceptably reproduced, as well as group of smaller amplitudes in the 100-300 s range.

SDG(8,5,5) See fig.s 4.5, 4.6, 4.7, 4.8. This source is capable of reproducing, for KANGIA tide gauge data, the presence of a smaller amplitude signal before the arrival of the greater one in marigrams 69 and 70. marigram 69 perfectly fits the amplitude of the greater positive signal, but fails in reproducing the first negative oscillation. This is actually achieved in virtual marigram 70, but the synthetic signal shows a sort of positive shift with respect to the data. Both waveform and amplitude of the first signals are not well reproduced in virtual marigrams 71 and 72. All synthetic marigrams show a shorter period than the signal recorded in KANGIA. The comparison between virtual marigram 212 and the data collected by ILULI shows that the the source reproduces well the first positive signal, but the amplitude and frequency of the subsequent signals are overestimated. As regards the spectral analysis, virtual marigram 212 shows peaks in the 200 s period, totally negligible in the observed data, and in the 300 s, present in the original data but overestimated by a factor greater than 5. Some amplitude peaks that are present in the data but not reproduced may be linked to Ilulissat harbor normal oscillation modes, that are not reproduced in virtual marigram 212 as expected. The two main amplitude peaks in virtual marigrams 69, 70, 71 and 72 coincide in period with the ones of KANGIA tide gauge, but underestimating the 2000 s \simeq 25 – 30 min and overestimating the 6000 s \simeq 1.5 h. Smaller amplitude peaks in the higher frequencies are

fairly reproduced, while all these virtual marigrams show spikes in the 200-800 s range, absent in the data.

SDG(9,6,2) See fig.s 4.9, 4.10, 4.11, 4.12. This source is similar to SDG(8,5,5), so this source will be analyzed in comparison with the previous one. The overall waveform of the synthetic marigrams are similar, with SDG(8,5,5) actually fitting better the first signal of marigrams 69 and 70. SDG(9,6,2) is capable of reproducing the amplitude of the first signal in virtual marigram 69 and the behavior of the signal for some oscillations after the negative peak in marigrams 69 and 71. In the spectral analysis, SDG(9,6,2) performs slightly better, in particular reducing the amplitude of the signals not present in the data. It is also interesting to notice that the amplitude of the main peak on most of the virtual marigrams is greater in SDG(8,5,5) than in SDG(9,6,2), even if the parameter a , governing the amplitude of the initial condition, is greater in the former.

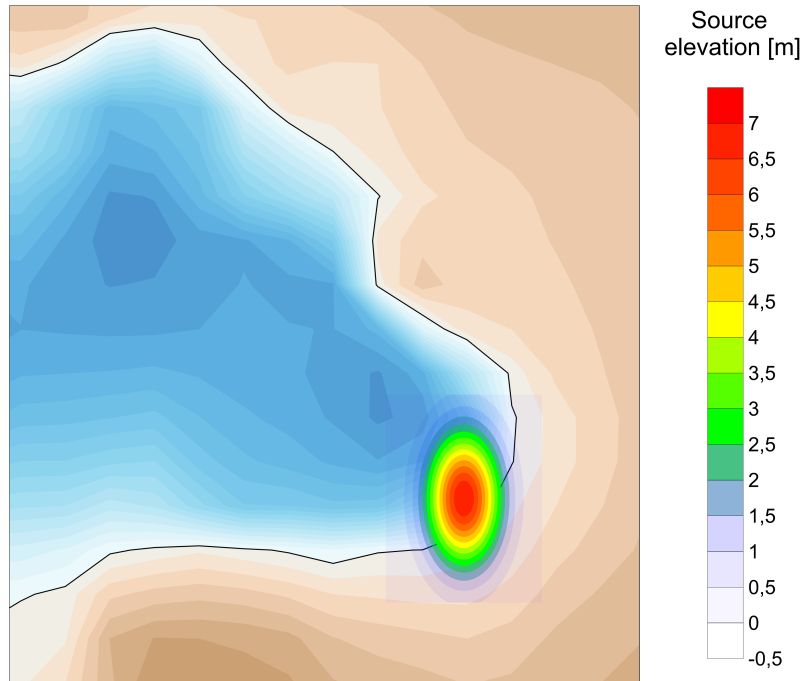
ADG(8,5,7,4) See fig.s 4.13, 4.14, 4.15, 4.16.

These results don't actually differ much from the ones obtained with the SDG sources. Virtual marigrams 69 and 70 reproduce well the waveform of the first minutes of signal, i.e. two positive peaks and a negative one. The amplitude of the main peak of virtual marigram 69 coincides with the one from KANGIA. Virtual marigram 70 reproduces the amplitudes of the positive and negative peaks with a positive shift. Virtual marigrams 71 and 72 fail at reproducing the waveform. The behavior of virtual marigram 212 is similar to the one seen with other sources. Overall, all the virtual marigrams show oscillations with a period shorter than the observed one. The spectral analysis shows results comparable to the ones of SDG(8,5,5): it has a good reproduction of the 2000 s \simeq 25 – 30 min and 6000 s \simeq 1.5 h period peaks, a decent reproduction of the shorter periods in the 200-800 s range and the insertion of unmatched amplitudes in the 500-1000 s range.

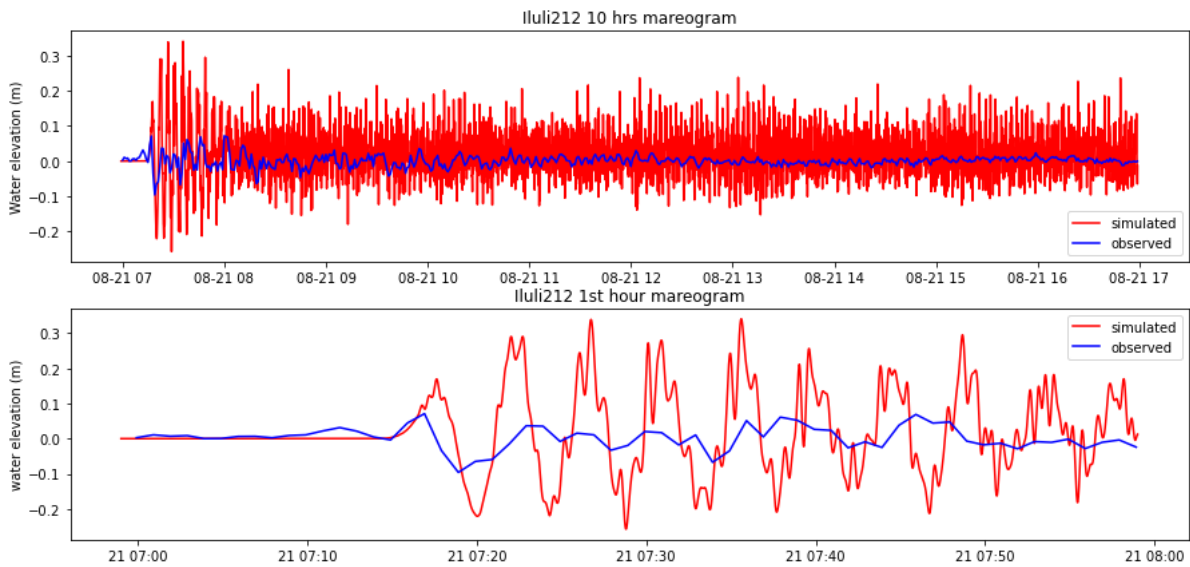
Comparison between best results Some considerations hold true for every source that has been presented here. The simulations have been set up to simulate 10 hours of signal propagation. The amplitude of the signal recorded in KANGIA and ILULI datasets dissipates faster than the simulated one, especially comparing the ILULI record and virtual marigram 212 (see fig.s 4.1b, 4.5b, 4.9b, 4.13b). This is probably due to the fact that UBO-TSUF D is based upon a non-dispersive model: the effect of dispersion can be neglected in the near field and over short distances, but has observable effects in the long time and distance propagation of waves. In none of the performed simulations the virtual marigram 72 showed decent results, thus suggesting its position to be way different to the one of KANGIA tide gauge. Also none of these results can properly reproduce the signal period, especially when modeling the initial signal.

Regarding the double gaussians, from fig.s 4.13a, 4.5a and 4.9 can be seen that part of the source negative values are on dry land. Other simulations, in which negative values

are in actual water grid points, required to move the source position, thus resulting in the addition of two more free parameters (i.e. the source x and y coordinates) and did not provide better results, so that path has not been pursued.

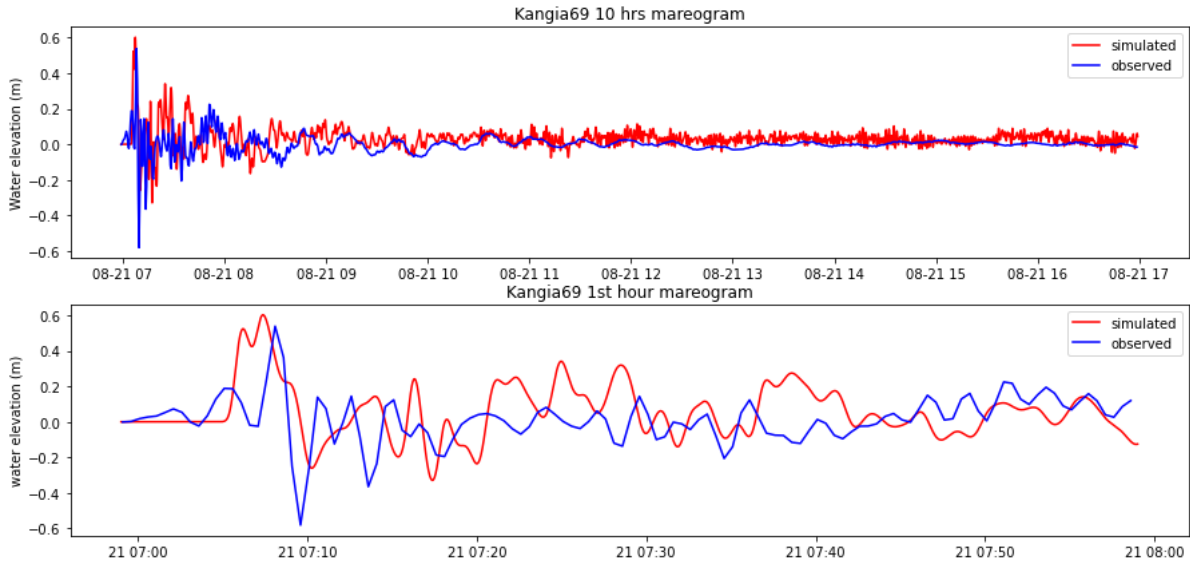


(a) *ASG(7,5,9) - Source function within the integration domain.*

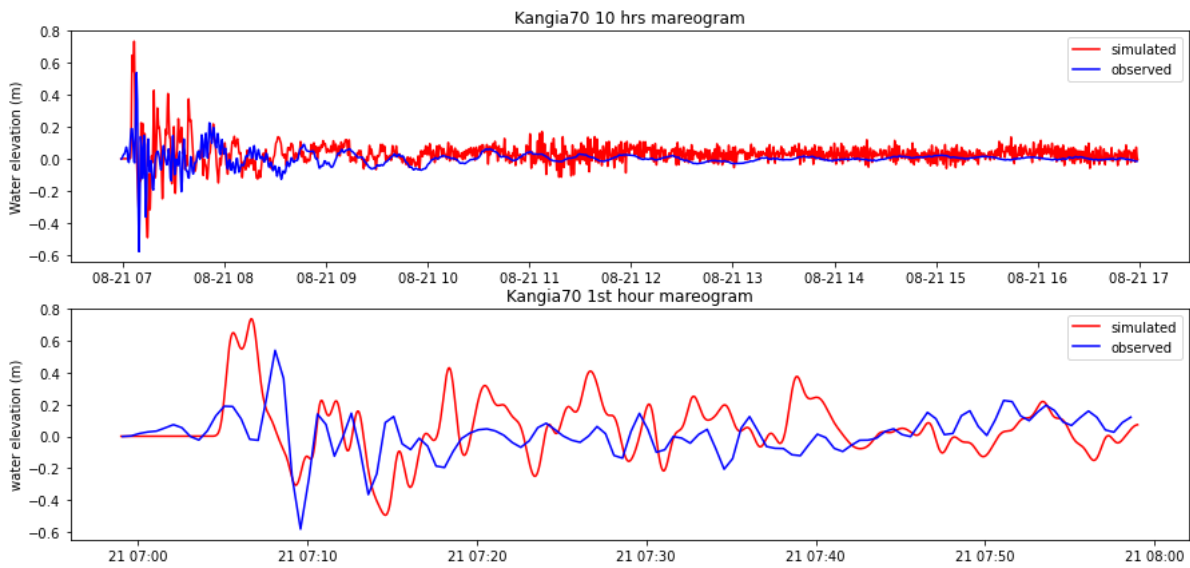


(b) *ASG(5,7,9)- ILULI real marigram (blue) vs virtual marigram 212 (red). Top: 10 hours signal. Bottom: first hour of signal.*

Figure 4.1: ASG(5,7,9) - a) Shape and position of the source function within the integration domain. b) Comparison between ILULI marigram and virtual marigram 212.

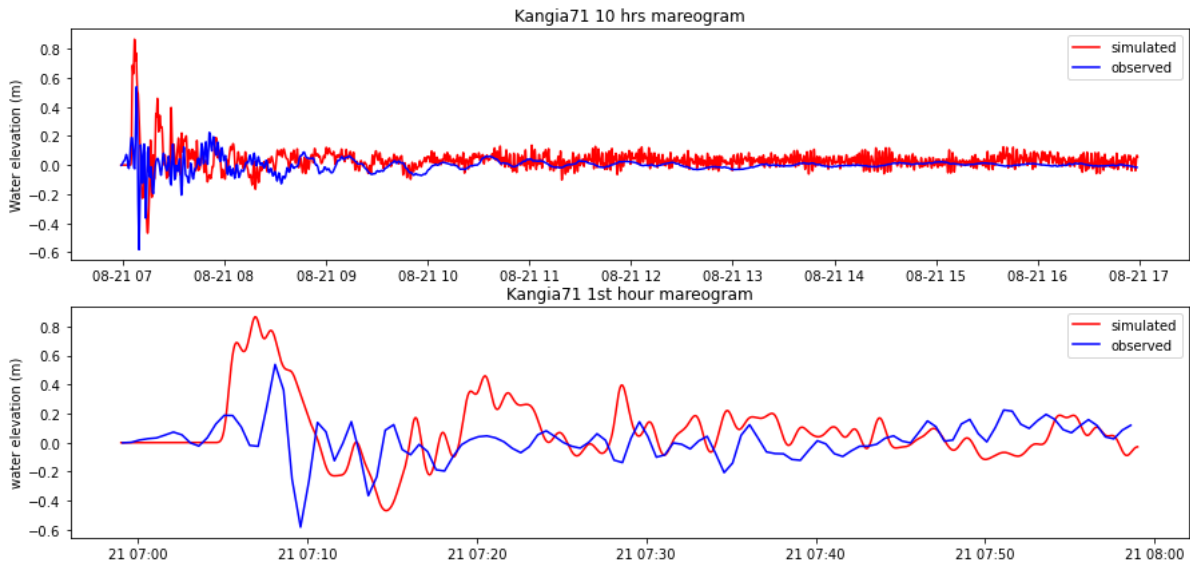


(a) ASG(5,7,9)- KANGIA real marigram (blue) vs virtual marigram 69 (red). Top: 10 hours signal. Bottom: first hour of signal.

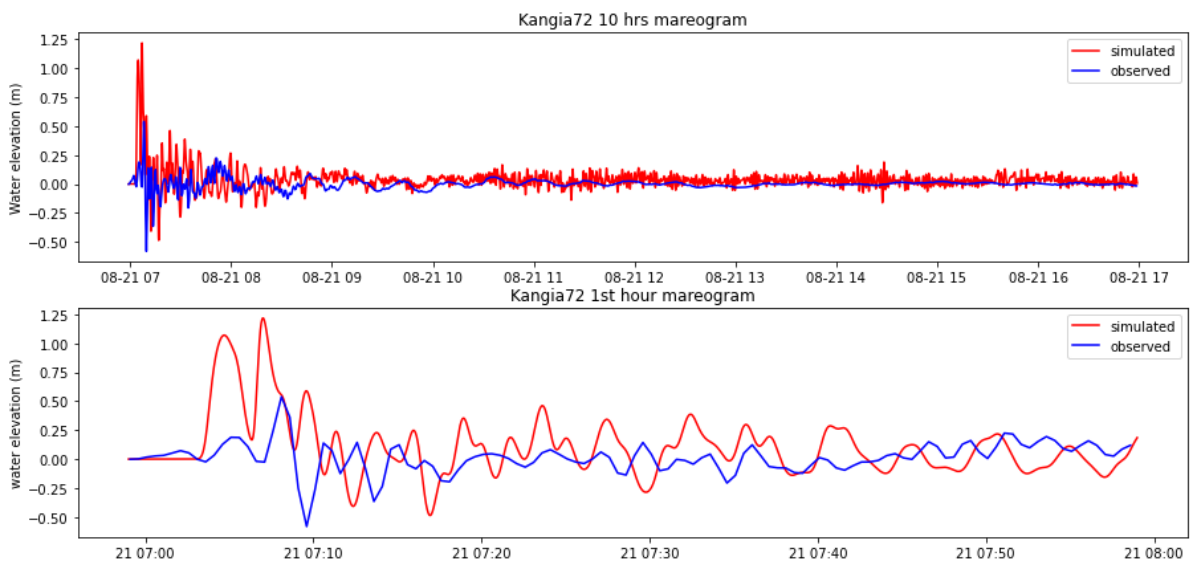


(b) ASG(5,7,9)- KANGIA real marigram (blue) vs virtual marigram 70 (red). Top: 10 hours signal. Bottom: first hour of signal.

Figure 4.2: ASG(5,7,9) - a) Comparison between KANGIA marigram and virtual marigram 69. b) Comparison between KANGIA marigram and virtual marigram 70.

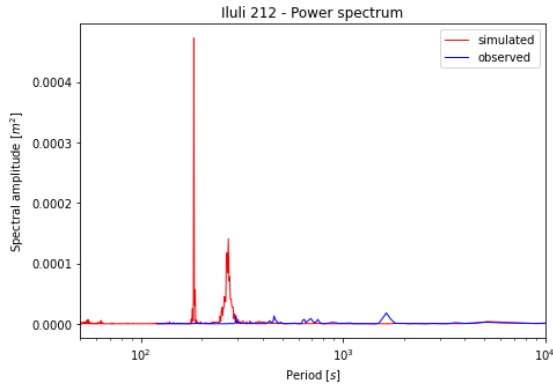


(a) ASG(5,7,9)- KANGIA real marigram (blue) vs virtual marigram 71 (red). Top: 10 hours signal. Bottom: first hour of signal.

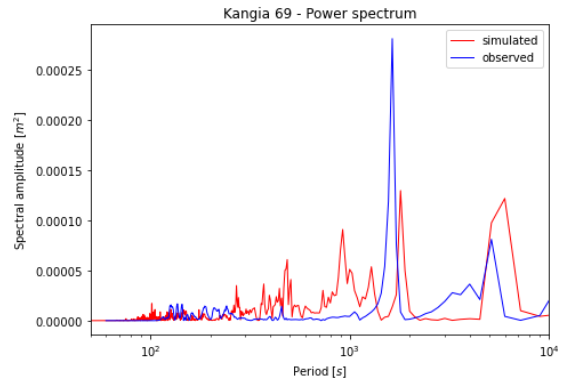


(b) ASG(5,7,9)- KANGIA real marigram (blue) vs virtual marigram 72 (red). Top: 10 hours signal. Bottom: first hour of signal.

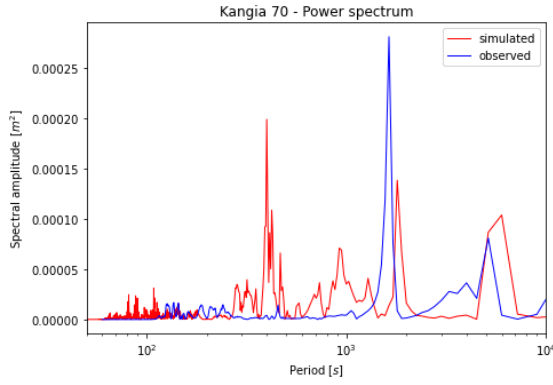
Figure 4.3: ASG(5,7,9) - a) Comparison between KANGIA marigram and virtual marigram 71. b) Comparison between KANGIA marigram and virtual marigram 72.



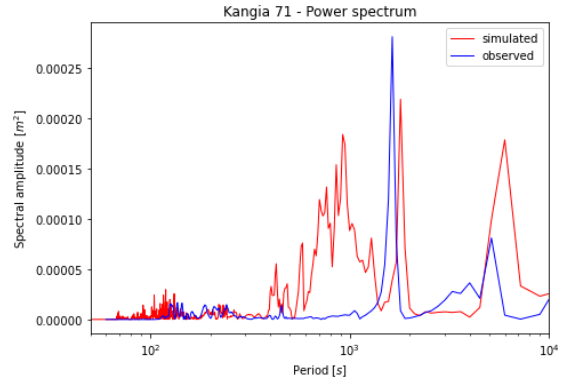
(a) $ASG(5,7,9)$ - Spectral amplitude: ILULI vs virtual marigram 212.



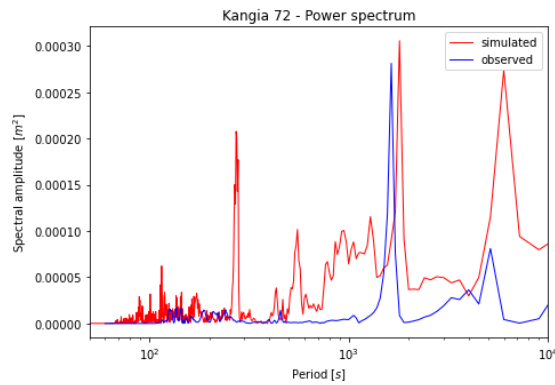
(b) $ASG(5,7,9)$ - Spectral amplitude: KANGIA vs virtual marigram 69.



(c) $ASG(5,7,9)$ - Spectral amplitude: KANGIA vs virtual marigram 70.

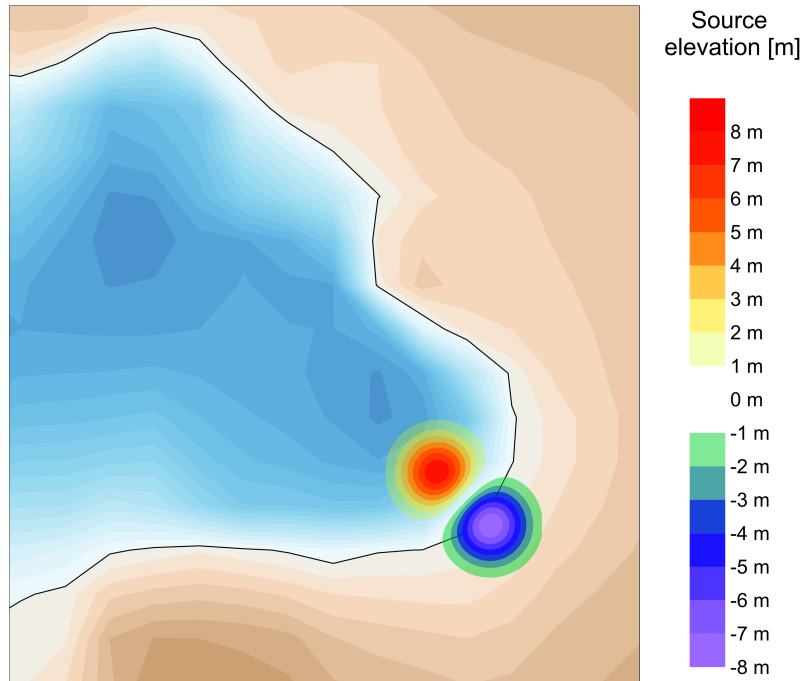


(d) $ASG(5,7,9)$ - Spectral amplitude: KANGIA vs virtual marigram 71.

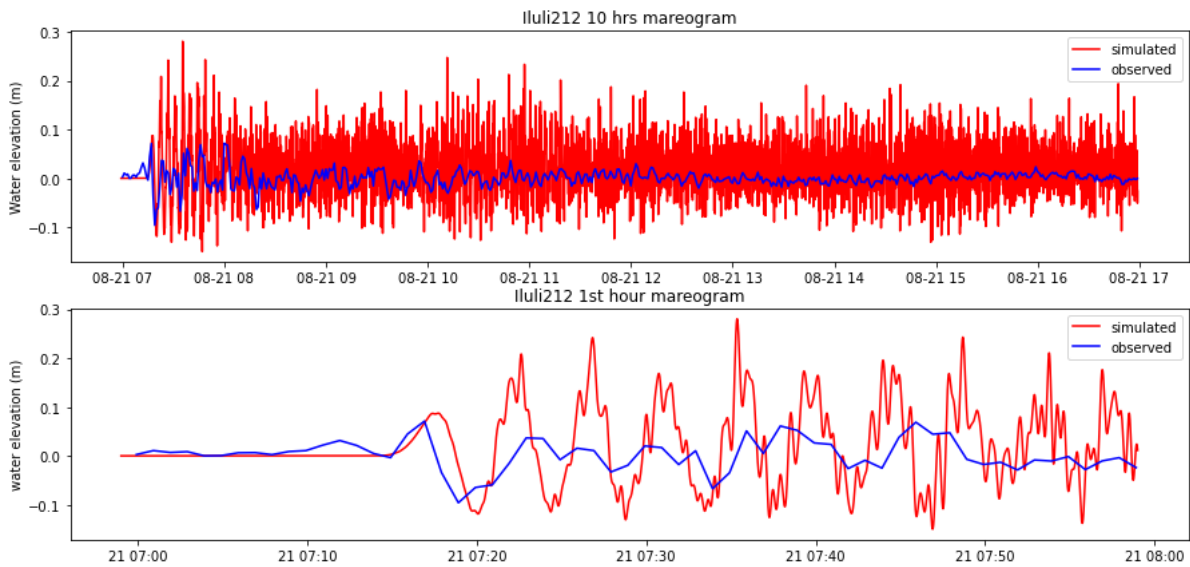


(e) $ASG(5,7,9)$ - Spectral amplitude: KANGIA vs virtual marigram 72.

Figure 4.4: $ASG(5,7,9)$ - Comparison between spectral amplitudes of the real signal (blue) and the virtual ones (red).

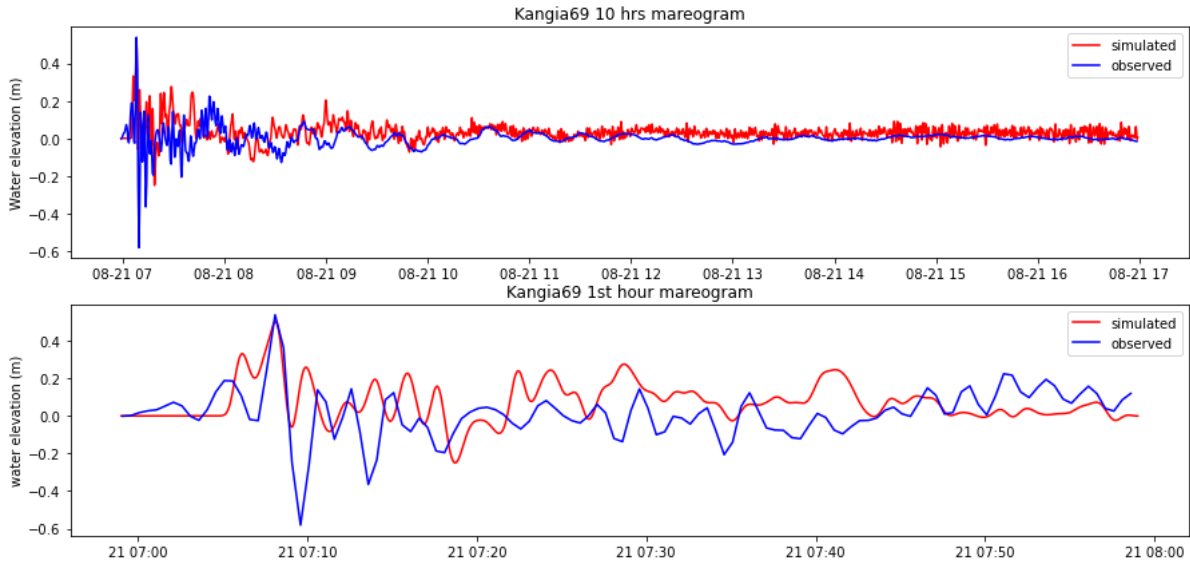


(a) $SDG(8,5,5)$ - Source function within the integration domain.

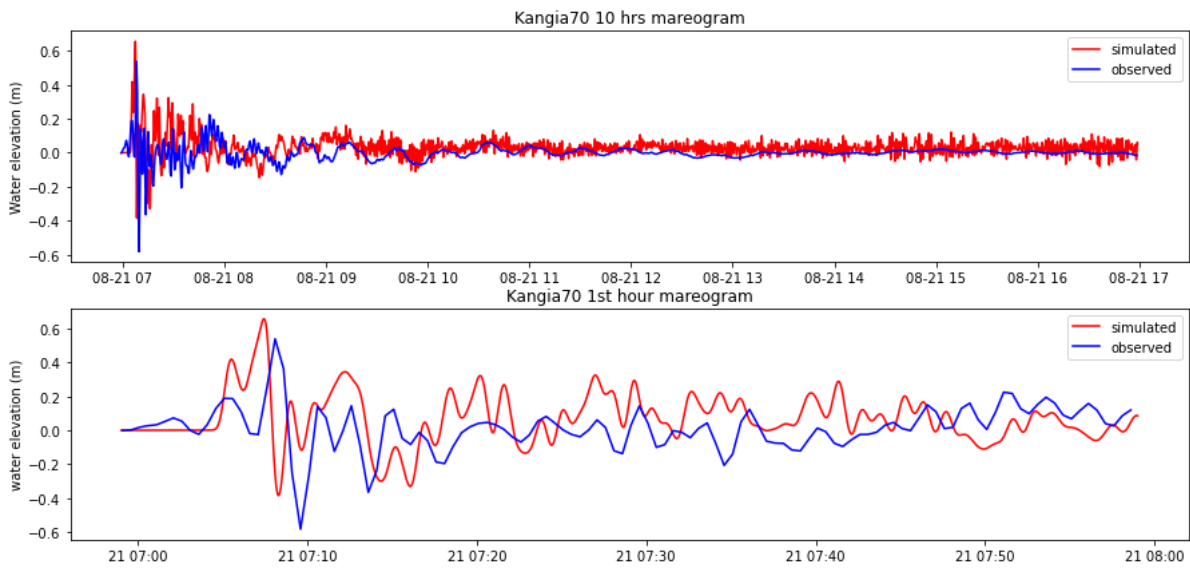


(b) $SDG(8,5,5)$ - ILULI real marigram (blue) vs virtual marigram 212 (red). Top: 10 hours signal. Bottom: first hour of signal.

Figure 4.5: $SDG(8,5,5)$ - a) Shape and position of the source function within the integration domain. b) Comparison between ILULI marigram and virtual marigram 212.

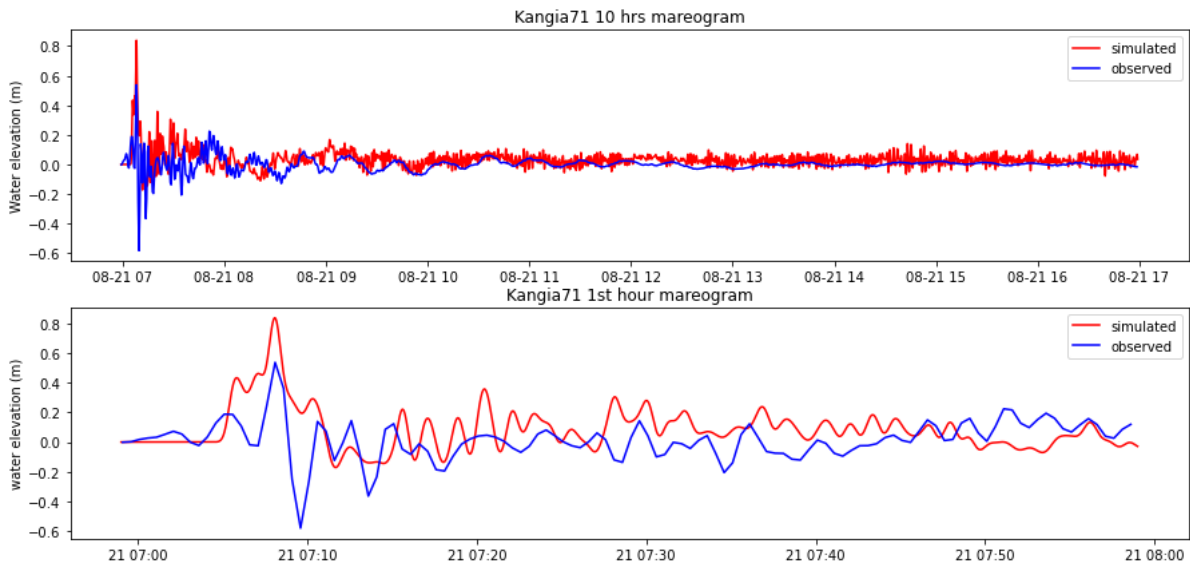


(a) $SDG(8,5,5)$ - KANGIA real marigram (blue) vs virtual marigram 69 (red). Top: 10 hours signal. Bottom: first hour of signal.

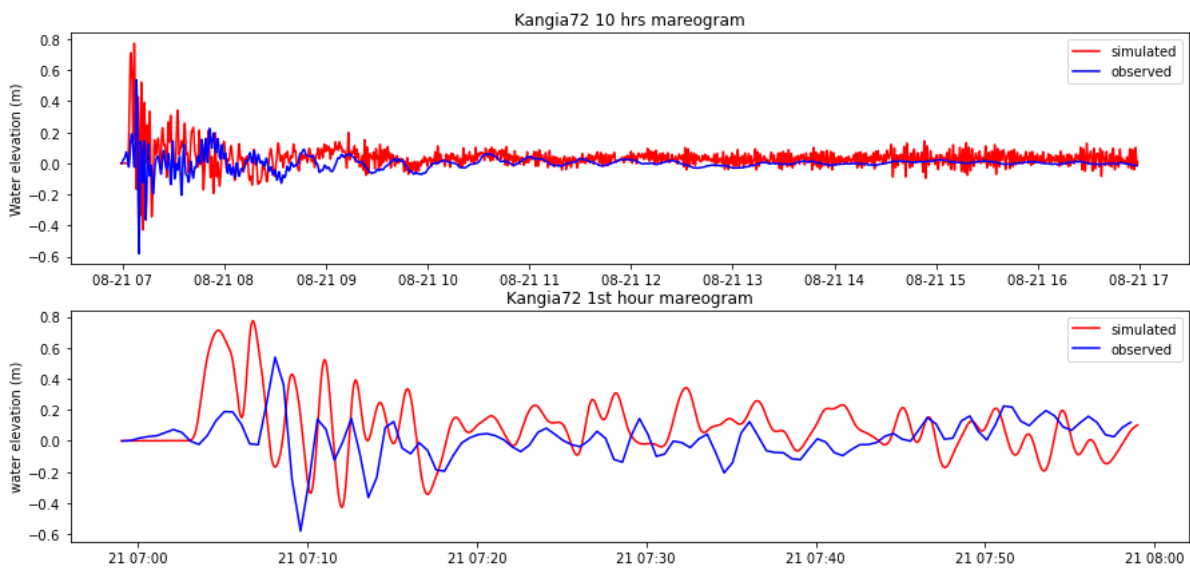


(b) $SDG(8,5,5)$ - KANGIA real marigram (blue) vs virtual marigram 70 (red). Top: 10 hours signal. Bottom: first hour of signal.

Figure 4.6: $SDG(8,5,5)$ - a) Comparison between KANGIA marigram and virtual marigram 69. b) Comparison between KANGIA marigram and virtual marigram 70.

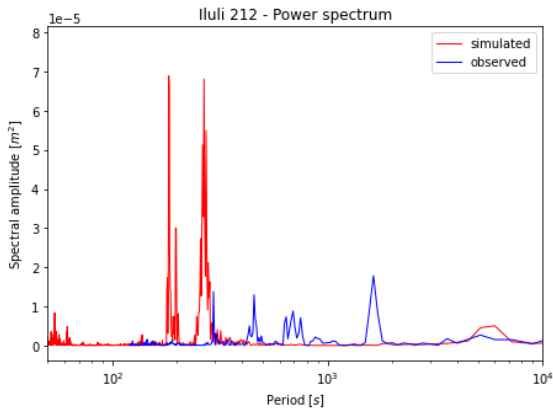


(a) $SDG(8,5,5)$ - KANGIA real marigram (blue) vs virtual marigram 71 (red). Top: 10 hours signal. Bottom: first hour of signal.

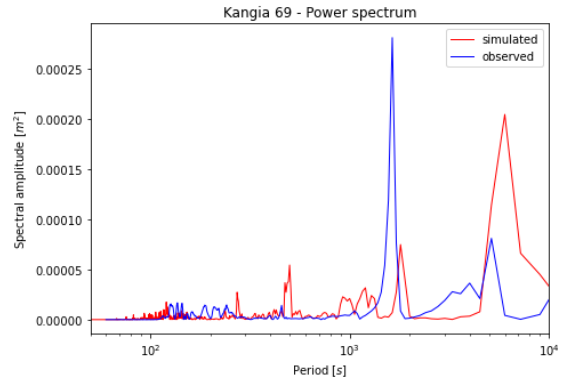


(b) $SDG(8,5,5)$ - KANGIA real marigram (blue) vs virtual marigram 72 (red). Top: 10 hours signal. Bottom: first hour of signal.

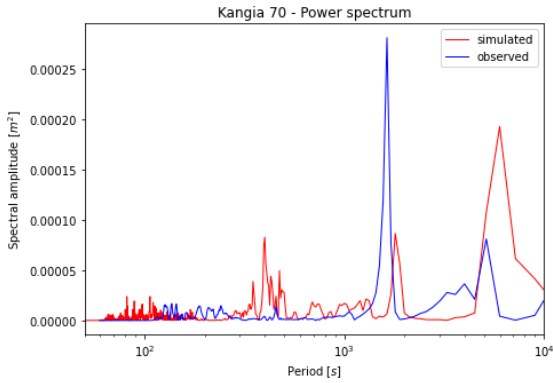
Figure 4.7: $SDG(8,5,5)$ - a) Comparison between KANGIA marigram and virtual marigram 71. b) Comparison between KANGIA marigram and virtual marigram 72.



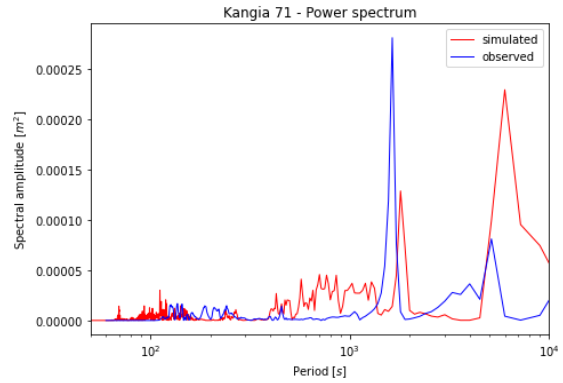
(a) *SDG(8,5,5)*- Spectral amplitude: *ILULI* vs virtual marigram 212.



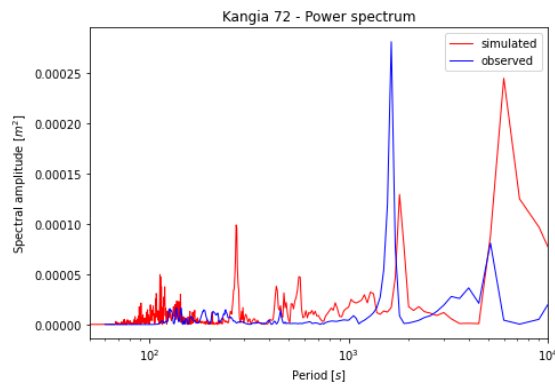
(b) *SDG(8,5,5)*- Spectral amplitude: *KANGIA* vs virtual marigram 69.



(c) *SDG(8,5,5)*- Spectral amplitude: *KANGIA* vs virtual marigram 70.

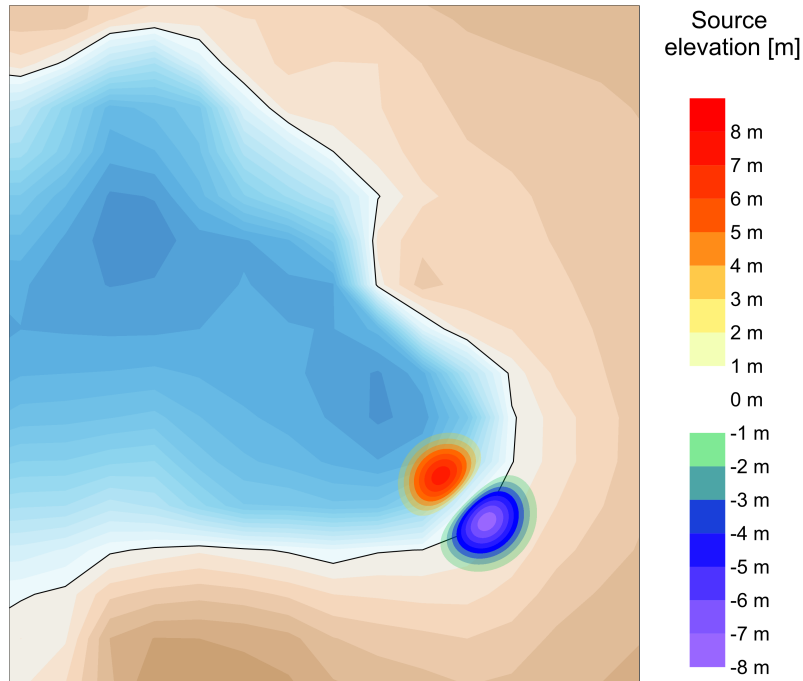


(d) *SDG(8,5,5)*- Spectral amplitude: *KANGIA* vs virtual marigram 71.

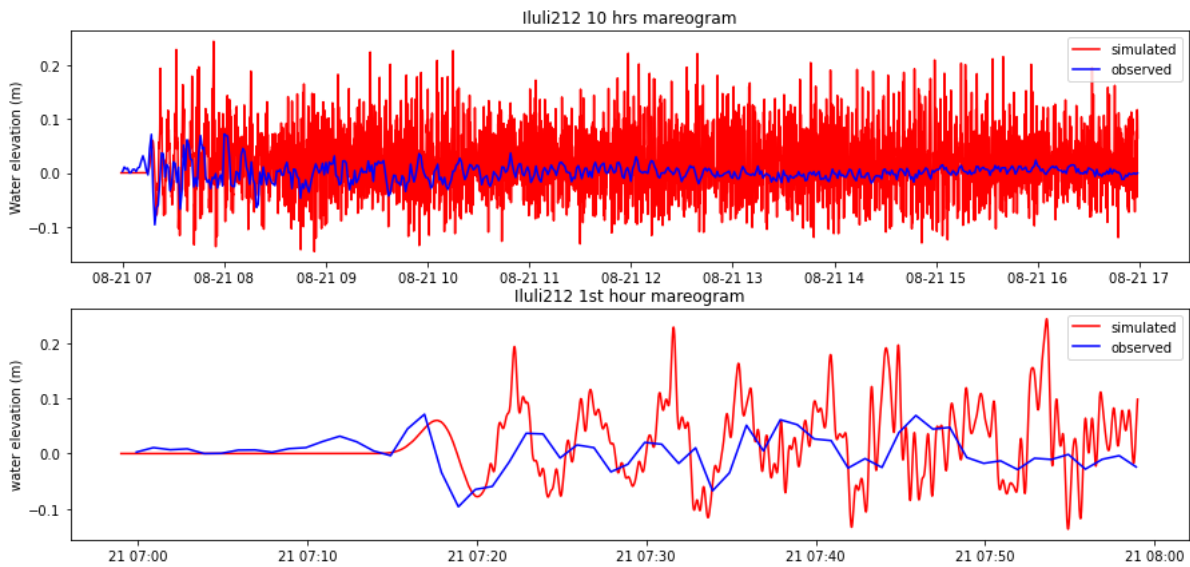


(e) *SDG(8,5,5)*- Spectral amplitude: *KANGIA* vs virtual marigram 72.

Figure 4.8: *SDG(8,5,5)* - Comparison between spectral amplitudes of the real signal (blue) and the virtual ones (red).

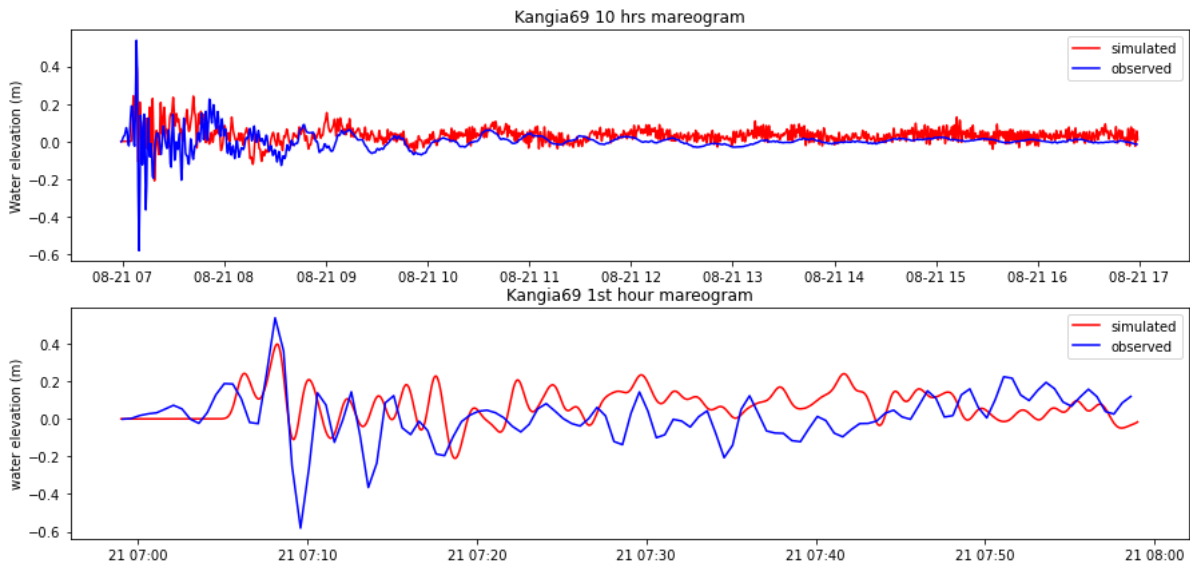


(a) $SDG(9,6,2)$ - Source function within the integration domain.

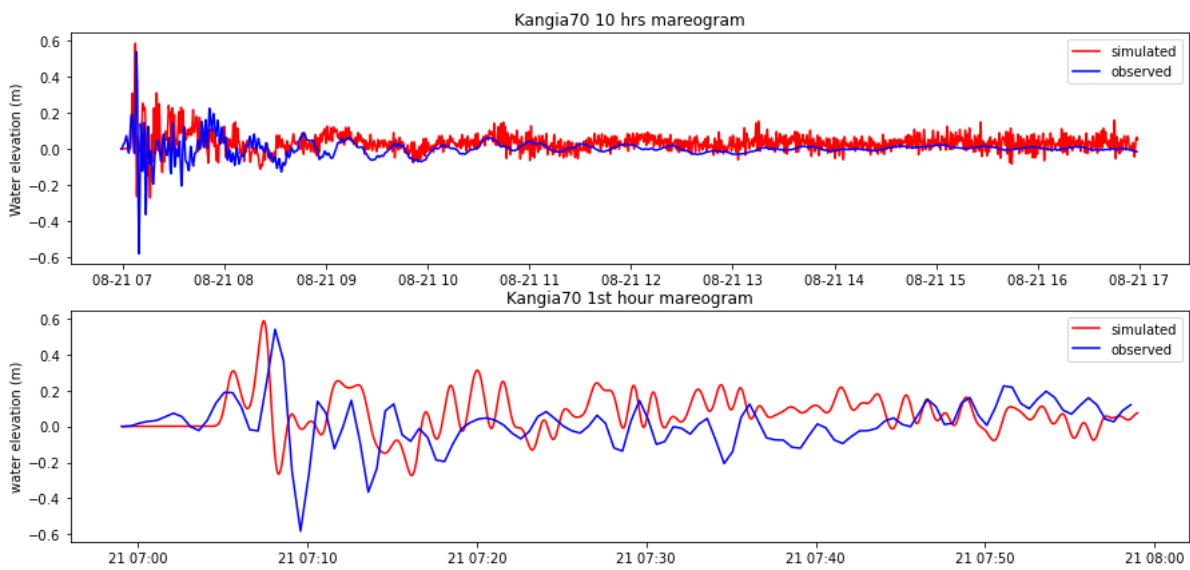


(b) $SDG(9,6,2)$ - ILULI real marigram (blue) vs virtual marigram 212 (red). Top: 10 hours signal. Bottom: first hour of signal.

Figure 4.9: $SDG(8,5,5)$ - a) Shape and position of the source function within the integration domain. b) Comparison between ILULI marigram and virtual marigram 212.

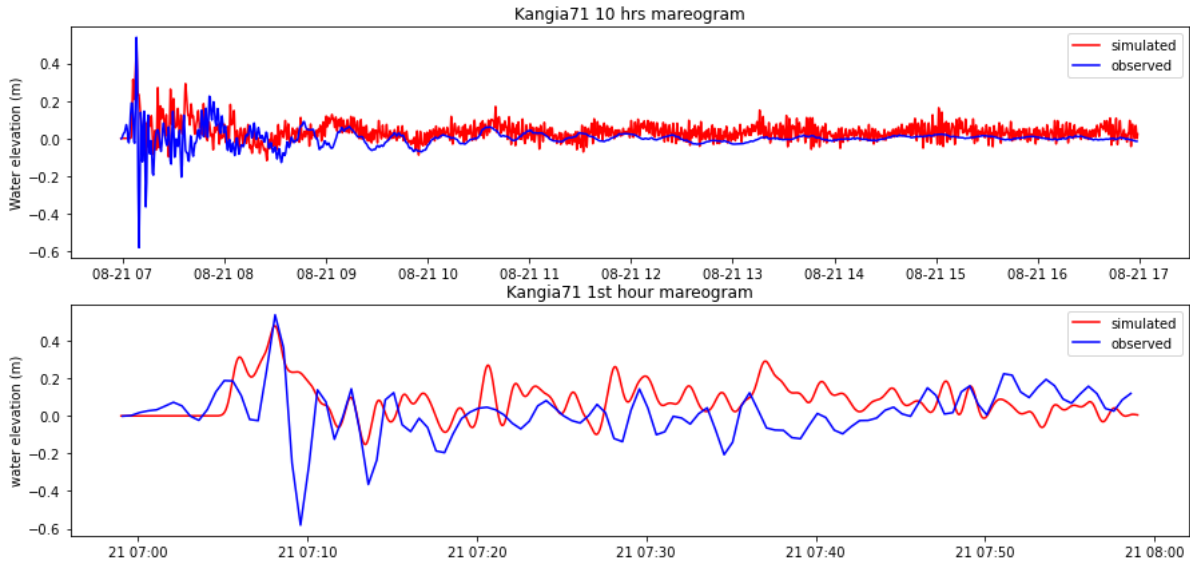


(a) $SDG(9,6,2)$ - KANGIA real marigram (blue) vs virtual marigram 69 (red). Top: 10 hours signal. Bottom: first hour of signal.

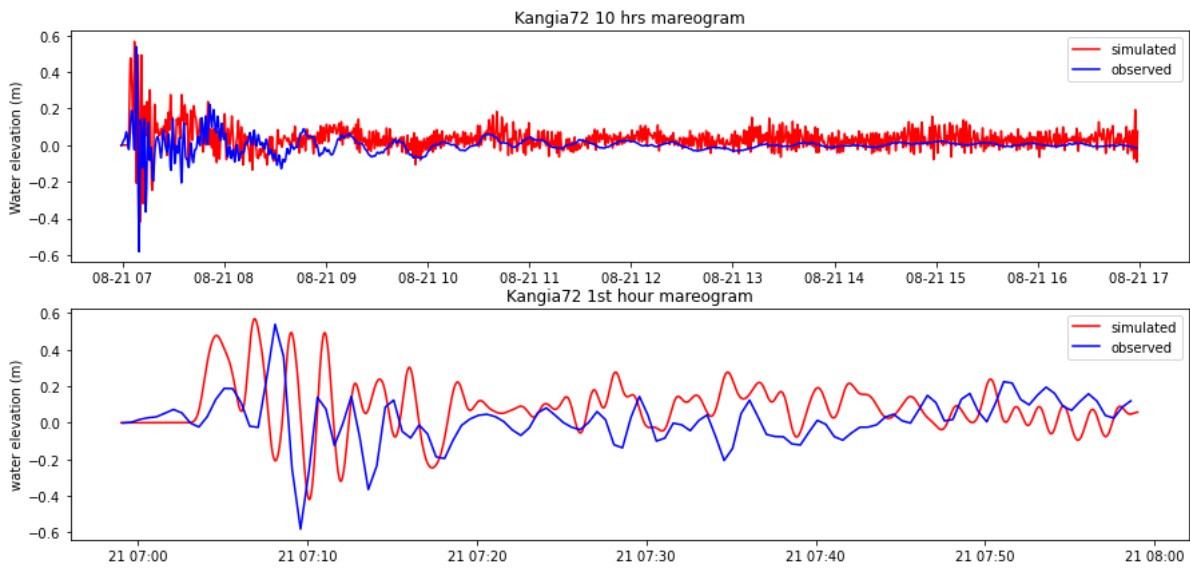


(b) $SDG(9,6,2)$ - KANGIA real marigram (blue) vs virtual marigram 70 (red). Top: 10 hours signal. Bottom: first hour of signal.

Figure 4.10: $SDG(9,6,2)$ - a) Comparison between KANGIA marigram and virtual marigram 69. b) Comparison between KANGIA marigram and virtual marigram 70.

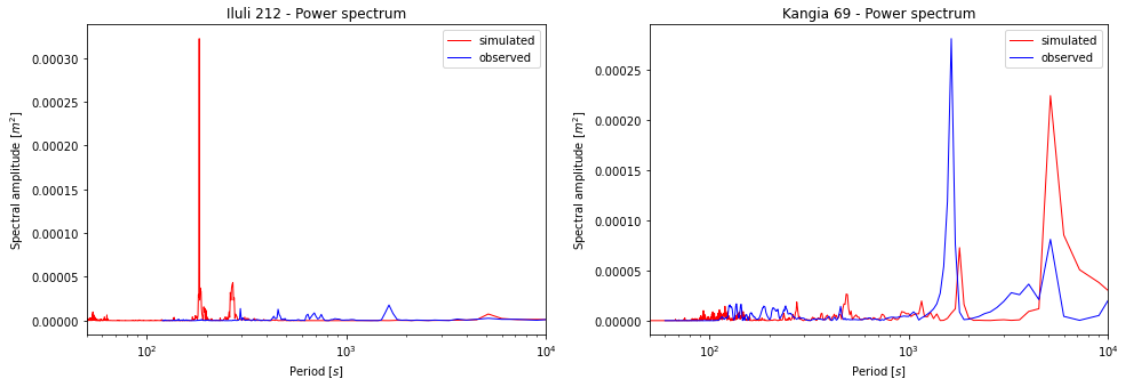


(a) $SDG(9,6,2)$ - KANGIA real marigram (blue) vs virtual marigram 71 (red). Top: 10 hours signal. Bottom: first hour of signal.

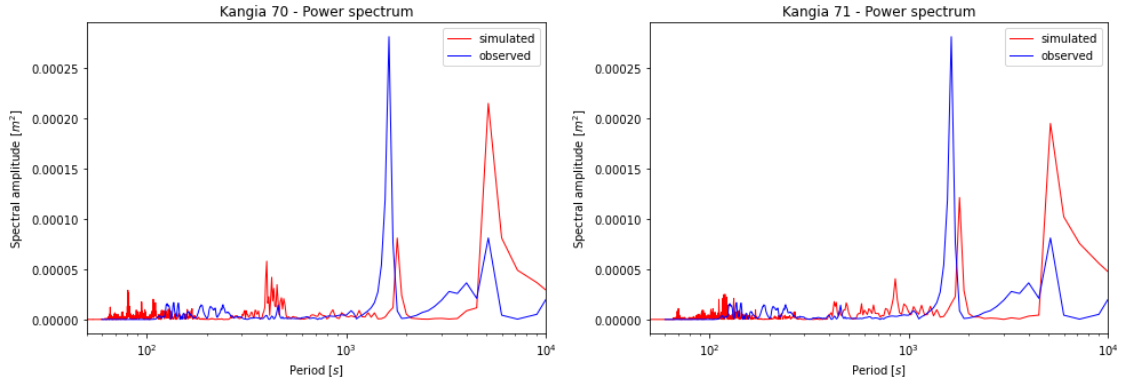


(b) $SDG(9,6,2)$ - KANGIA real marigram (blue) vs virtual marigram 72 (red). Top: 10 hours signal. Bottom: first hour of signal.

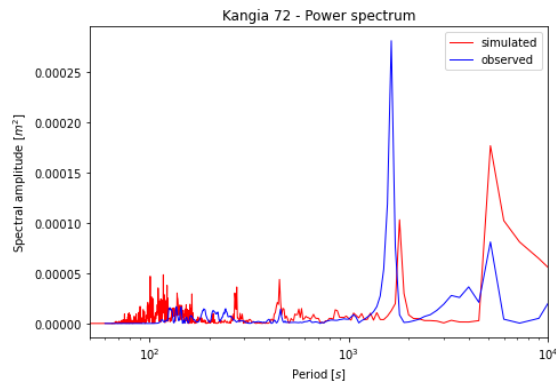
Figure 4.11: $SDG(9,6,2)$ - a) Comparison between KANGIA marigram and virtual marigram 71. b) Comparison between KANGIA marigram and virtual marigram 72.



(a) *SDG(9,6,2)*- Spectral amplitude: ILULI vs virtual marigram 212. (b) *SDG(9,6,2)*- Spectral amplitude: KANGIA vs virtual marigram 69.

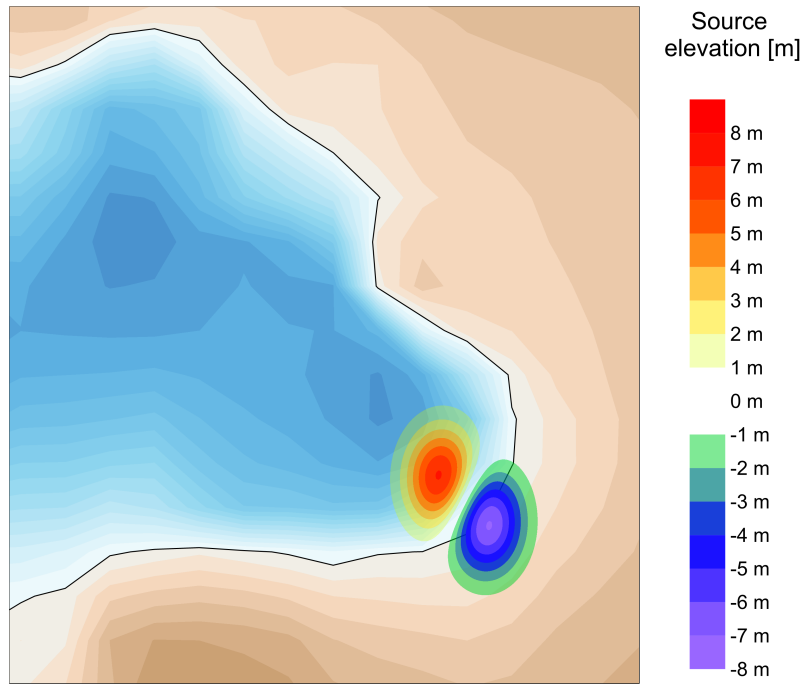


(c) *SDG(9,6,2)*- Spectral amplitude: KANGIA vs virtual marigram 70. (d) *SDG(9,6,2)*- Spectral amplitude: KANGIA vs virtual marigram 71.

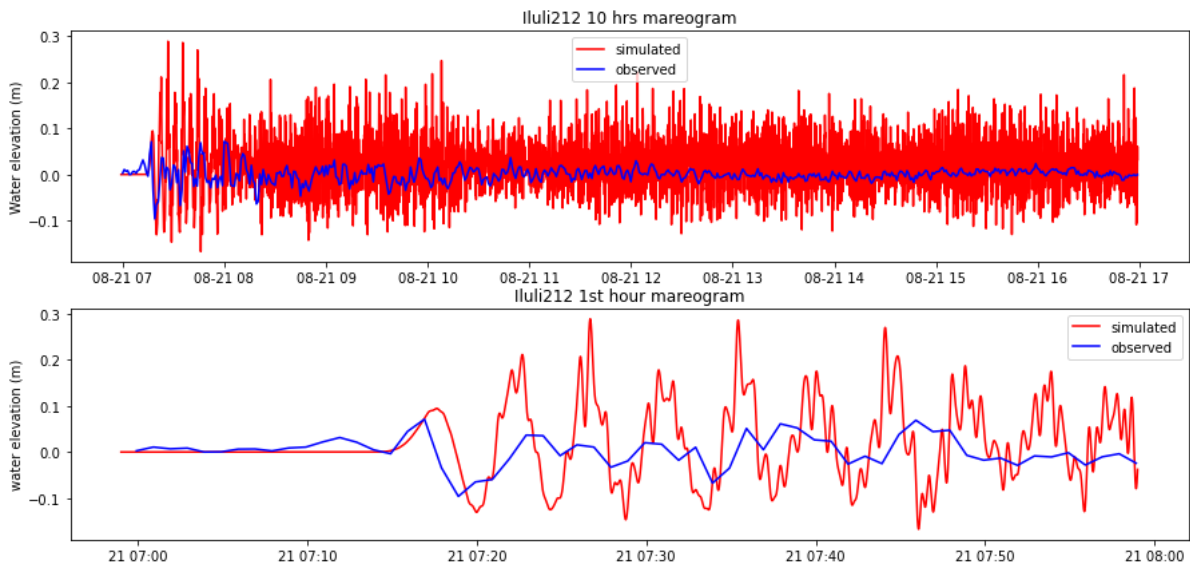


(e) *SDG(9,6,2)*- Spectral amplitude: KANGIA vs virtual marigram 72.

Figure 4.12: *SDG(9,6,2)* - Comparison between spectral amplitudes of the real signal (blue) and the virtual ones (red).

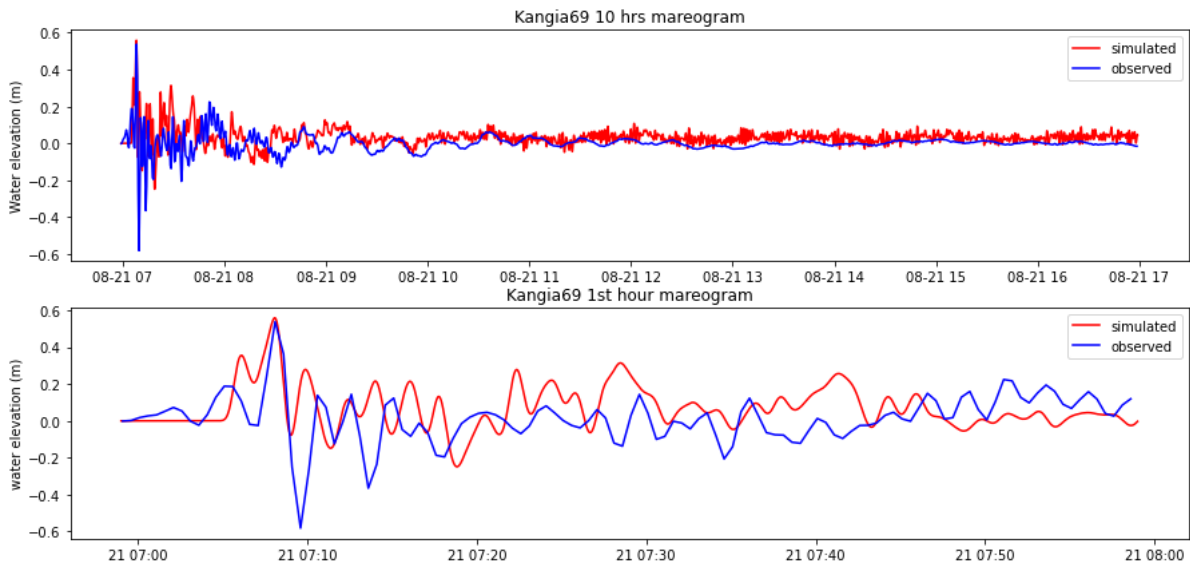


(a) $ADG(8,5,7,4)$ - Source function within the integration domain.

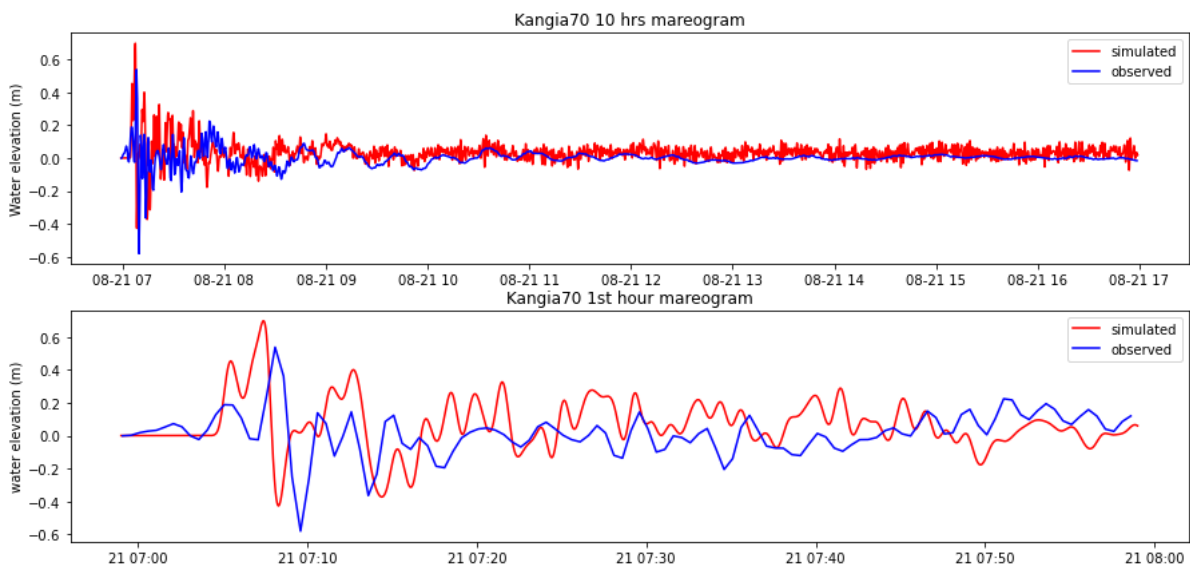


(b) $ADG(8,5,7,4)$ - ILULI real marigram (blue) vs virtual marigram 212 (red). Top: 10 hours signal. Bottom: first hour of signal.

Figure 4.13: $ADG(8,5,7,4)$ - a) Shape and position of the source function within the integration domain. b) Comparison between ILULI marigram and virtual marigram 212.

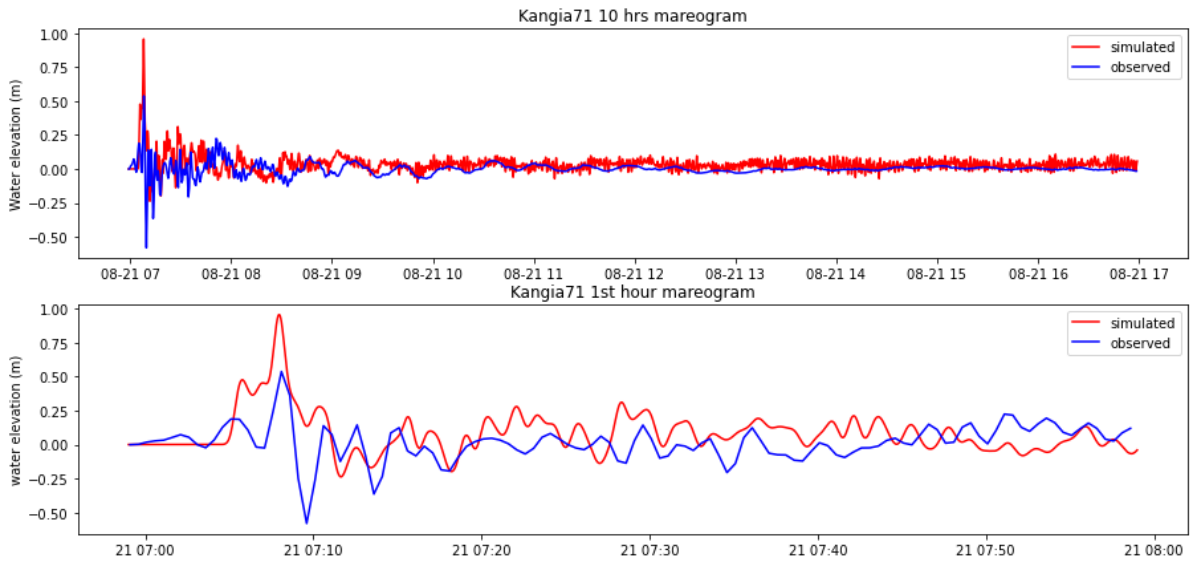


(a) $ADG(8,5,7,4)$ - KANGIA real marigram (blue) vs virtual marigram 69 (red). Top: 10 hours signal. Bottom: first hour of signal.

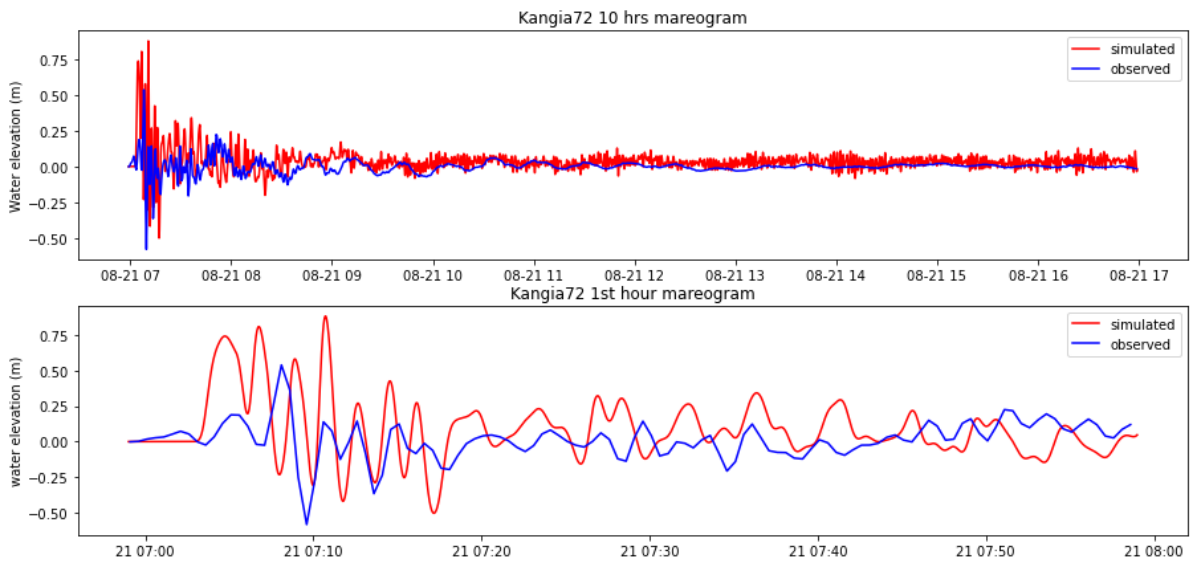


(b) $ADG(8,5,7,4)$ - KANGIA real marigram (blue) vs virtual marigram 70 (red). Top: 10 hours signal. Bottom: first hour of signal.

Figure 4.14: $ADG(8,5,7,4)$ - a) Comparison between KANGIA marigram and virtual marigram 69. b) Comparison between KANGIA marigram and virtual marigram 70.

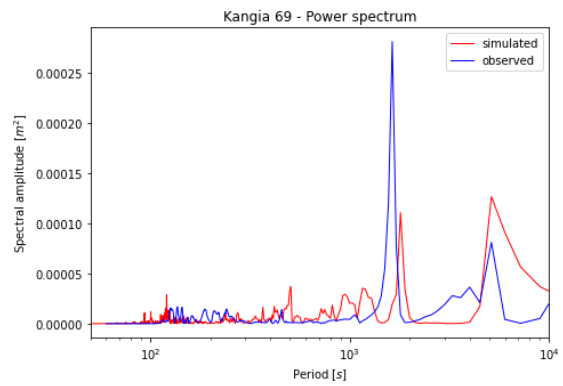
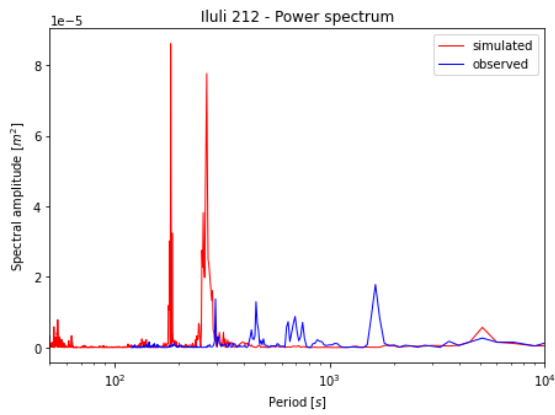


(a) $ADG(8,5,7,4)$ - KANGIA real marigram (blue) vs virtual marigram 71 (red). Top: 10 hours signal. Bottom: first hour of signal.

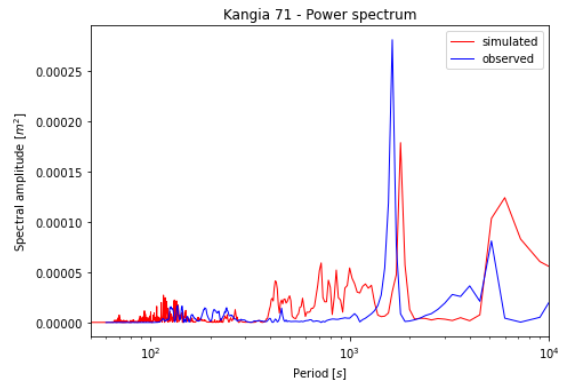
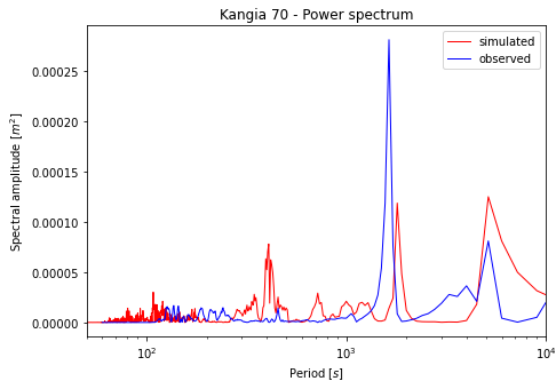


(b) $ADG(8,5,7,4)$ - KANGIA real marigram (blue) vs virtual marigram 72 (red). Top: 10 hours signal. Bottom: first hour of signal.

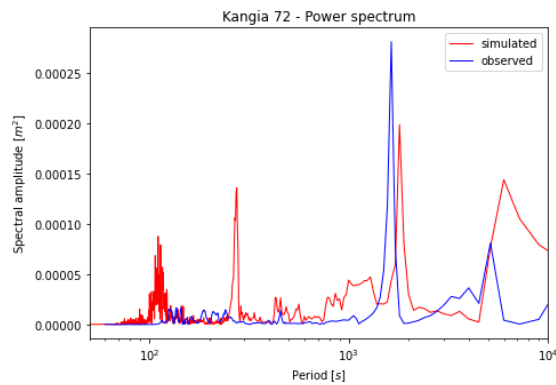
Figure 4.15: $ADG(8,5,7,4)$ - a) Comparison between KANGIA marigram and virtual marigram 71. b) Comparison between KANGIA marigram and virtual marigram 72.



(a) $ADG(8,5,7,4)$ - Spectral amplitude: ILULI vs virtual marigram 212. (b) $ADG(8,5,7,4)$ - Spectral amplitude: KANGIA vs virtual marigram 69.



(c) $ADG(8,5,7,4)$ - Spectral amplitude: KANGIA vs virtual marigram 70. (d) $ADG(8,5,7,4)$ - Spectral amplitude: KANGIA vs virtual marigram 71.



(e) $ADG(8,5,7,4)$ - Spectral amplitude: KANGIA vs virtual marigram 72.

Figure 4.16: $ADG(8,5,7,4)$ - Comparison between spectral amplitudes of the real signal (blue) and the virtual ones (red).

Chapter 5

Conclusions

The main objective of this investigation is to investigate possible sources for calving-generated tsunamis. In all signal propagation phenomena the source is dependent upon some characteristics of the generating event, thus if the initial condition of a calving-generated tsunami is known, it is possible to infer information about the characteristics of the calved iceberg (e.g. dimensions, mass, calving mechanism). Three different source functions, each one dependent upon three or four parameters, have been tested in the attempt to reproduce the signal generated by a calving tsunami occurred on August 21st 2009 in Jakobshavn Isbræ, Western Greenland. The tested sources are the Asymmetric Single Gaussian (ASG) and the Symmetric Double Gaussian (SDG), depending upon three parameters, and the Asymmetric Double Gaussian (ADG), depending upon four parameters. All these are described in chapter 3. These sources have been tested as initial conditions for the UBO-TSUFDF code, comparing the results of virtual marigrams to the data collected by two tide gauges: KANGIA, located within the fjord and relatively close to the calving front, and ILULI, located in the harbor of the town of Ilulissat, near the seamount of the fjord. Several combinations of the parameter values have been investigated in order to find the ones that could better fit the data. The best result for each simulation have been reported and discussed in chapter 4. Acknowledging the results, now conclusions will be carried.

It has proven difficult to actually fit the simulations to the data. Tsunami waves are non-linear, so it is not easy to foresee how a change in the value of a parameter would effect the results of a simulation. Moreover, there are not clear constraints on the values of the parameters, thus the adopted approach was very explorative. Probably there are combinations of parameter values that have not been tested and could possibly result in a better agreement between real and synthetic marigrams, so it is safer to treat any conclusion drawn from this work as not definitive.

The ASG source produced worse results than the other sources. Such cases couldn't be able to reproduce the first impulse recorded in KANGIA tide gauge to an acceptable degree, not correctly fitting the signal waveform, overestimating its amplitude and not

matching the arrival time of the different peaks. The polarity and amplitude of the first impulse recorded in ILULI are correctly reproduced, but the period of the following waves is underestimated. Spectral analysis showed that the synthetic signals could acceptably reproduce the two main amplitude peaks of the data, with periods of 2000 s and 5000 s, but added more high-amplitude signals, not present in the original data, in the 500 – 1000s period range. The SDG and ADG produced similar results. In KANGIA, both sources could be able to acceptably reproduce polarity and amplitude of the first arriving impulses, but failing in reproducing the correct time interval between different wave peaks. In ILULI these sources have a behavior similar to the ASG, reproducing correctly polarity, amplitude and arrival time of the first signal, but not correctly fitting amplitude and period of the following signals. Spectral analysis of the virtual marigrams produced using these sources brought results similar to the ones obtained using ASG: the two main peaks at 2000 s and 5000 s periods and some smaller amplitude peak in the shorter periods are well fit, but the simulations added more high-amplitude signals in the 500 – 1000s period range.

SDG and ADG performed better than the ASG, and this may be due to the actual nature of the considered calving event: the overturning movement of the capsizing iceberg is effectively observed generating a positive amplitude impulse on the emerging side, while generating a negative amplitude impulse on the submerging side, and is thus better represented by these two sources. Due to its shape the ASG might be more appropriate in modeling buoyancy or gravity-driven fall, with positive amplitude the former, with negative amplitude the latter.

SDG and ADG have comparable results. ADG source needs one parameter more than SDG, thus being more complex. This added complexity is not matched by a significant improvement in the results, so Occam’s razor principle (or Von Neumann’s elephant statement reported in Dyson 2004) suggests that SDG should be a preferred source between the two.

Further developments

Several improvements could be made to validate or disprove the conclusions of this work. Clearly, repeating the investigation using better data could improve the quality of the results. Tide gauges with a greater sampling rate could reduce aliasing effects, while a better geolocalization of the tide gauges could easily increase the efficiency in evaluating the results by reducing the number of virtual marigrams that have to be produced and inspected. Moreover, a better representation of the bathymetry of the fjord, specially in proximity of the calving front, could allow to create a more realistic computational grid. Also, seismic data from the Greenland Ice Sheet Monitoring Network (GLISN) could be used to analyze the impact of the tsunami on the coast.

As previously said, there might be combinations of parameter values that could lead

to better results, specially fo ADG, possibly leading to different conclusions. In order to cross-validate these results, similar tests should be conducted with other events, both in Jakobshavn Isbræ and similar places. Moreover, there are several possible sources that have not been considered in this work that might as well be tested. Between those, even time-dependent sources should be considered as the capsizing of the glacier is not really an instantaneous process. Another possible path that I would like to suggest is to investigate correlations between the tsunami and the glacial earthquake sources generated by the same calving event. Further improvement in numerical modeling could be made using codes based upon a dispersive model, thus allowing to better reconstruct the long-term behavior of the signal. An interesting development would be the search of correlations between the values of the source parameters and the characteristics of the calved iceberg. In order to prove or disprove this, the same source functions have to be tested with events of similar calving mechanism.

As a final word, the hope is that the conclusions derived from this work could possibly lead to a further advance in the understanding of the calving problem and all of its related phenomena.

Ringraziamenti

Quando ho scritto la tesi per la triennale, ho finito le ultime correzioni mezz'ora prima dello scadere del countdown, non facendo in tempo a scrivere i ringraziamenti. Questa volta ho ben cinque ore!

Il primo ringraziamento va al prof. Filippo Zaniboni per tutto il supporto che mi ha dato con questa tesi: sei sempre stato presente e disponibile. Grazie per le correzioni e i suggerimenti, per il permesso di usare UBO-TSUF_D, grazie per avermi insegnato a surfare in mezzo ai fiordi. Un ringraziamento speciale al prof Alberto Armigliato per avermi consentito di utilizzare il server del Dipartimento di Geofisica per le simulazioni, facendomi veramente risparmiare un sacco di tempo. Ci ho lasciato dentro 61 GB di dati! Vorrei inoltre ringraziare tutti i professori di FST che mi hanno insegnato in questi anni, tutti sempre competenti e disponibili. Un ringraziamento anche al professor Jason Amundson della University of Alaska Southeast per aver fornito i dati dei mareografi.

Grazie mamma e babbo. Grazie di tutto. Ma davvero, di tutto. Non sto qui a spiegarvi cosa avete fatto per me, lo sapete benissimo. Mi avete dato l'opportunità di studiare e vivere a Bolo e di provare esperienze nuove. Mi avete dato i doverosissimi calci di cui avevo bisogno, mi date un amore infinito. Grazie. Grazie Pilli per essere la complice perfetta, continuiamo a ridere e a divertirci_(EDPG).

Melli, grazie. Ci sono troppe cose da dire e non sto a scriverle qui. Hai visto ogni alto e basso di questo percorso, e sei stata sempre lì con me. Qualsiasi strada cammineremo, la cammineremo mano nella mano ridendo.

Grazie nonna Anna e nonno Sandro, grazie Nonno Vittorio, non vi siete mai risparmiati una fatica per noi. Grazie nonna Rosi. Saresti così di contenta di me adesso, mi avresti detto "Che brev 'l mi coc!" e mi avresti abbracciato fortissimo. Grazie per tutto l'amore che mi hai dato. Grazie zio Fedi e zio Giù, siete due colonne portanti della mia crescita. Grazie anche ad Andri e Ale, siate coraggiosi, impegnatevi e spaccate tutto. Una coccola anche alla Maia, che con tutto ciò che le ho ripetuto può tranquillamente laurearsi in fisica senza studiare.

Grazie Magno e Daddi. Siete stati dei compagni di vita fenomenali. Se sono un po' più adulto è anche merito vostro. Grazie Cri per il $\pi\omega\nu\omega\mu\epsilon\nu$, grazie Torfi per l'affetto. Grazie Maso, Blaso e Lollo. Grazie agli eroi che hanno impugnato le asce al mio fianco. Grazie a Adhara, Gino, Harren, Istaril, Malibuk, MdC, Nevitash, Sailas. Grazie a colui che ha

dato vita a questo mondo. Grazie Franci e Calcio per essere stati sempre disponibili per un aiuto e per aver continuato a stimolare la mia passione per la fisica.

Grazie Marco, ti voglio bene. Spero che la vita ti porti il meglio, e voglio essere lì con te per vederlo. Grazie Ama, Bigo e Marti. AO. Grazie Pasqua, sono contento di essermi avvicinato così tanto a te. Grazie avventurieri della Fondazione Pietraviva, o qualsiasi cosa siate diventati ora. Mi sento come una mamma aquila che vede i suoi aquilotti prendere il volo e librarsi nell'aria.

E infine, grazie ai miei compagni terrestri. Grazie Benni, Proietz, Carol, Lele, Cesare, l'Anna e Jack. Mi avete accompagnato in questa avventura fatta di studio, di sudore, di festa. Mi sono sentito in una famiglia (mamma Carols e i figli che la fanno arrabbiare). Grazie, spaccate tutto e buona fortuna!

Bibliography

- Alley, Richard B. et al. (2008). “A Simple Law for Ice-Shelf Calving”. In: *Science* 322.
- Amundson, J. M. et al. (2008). “Glacier, fjord, and seismic response to recent large calving events, Jakobshavn Isbræ, Greenland”. In: *Geophysical Research Letters* 35.
- Amundson, J. M. et al. (2010). “Ice mélange dynamics and implications for terminus stability, Jakobshavn Isbræ, Greenland”. In: *Journal of Geophysical Research: Earth Surface* 115.
- Amundson, Jason M. et al. (2012). “Observing calving-generated ocean waves with coastal broadband seismometers, Jakobshavn Isbræ, Greenland”. In: *Annals of glaciology* 53.
- Bassis, J. N. (2011). “The statistical physics of iceberg calving and the emergence of universal calving laws”. In: *Journal of Glaciology* 57.
- Batchelor, G. K. (1967). *An Introduction to Fluid Dynamics*. New York: Cambridge university press.
- Benn, Douglas I. and Jan A. Åström (2018). “Calving glaciers and ice shelves”. In: *Advances in Physics X*.
- Benn, Douglas I. et al. (2007). “Calving processes and the dynamics of calving glaciers”. In: *Earth science reviews*.
- Broeke, Michiel van den et al. (2009). “Partitioning recent Greenland Mass Loss”. In: *Science* 326.
- Brown, C. S. et al. (1982). “Calving Speed of Alaska Tidewater Glaciers, With Application to Columbia Glacier”. In: *United States Geological Survey Professional Paper*.
- Dahl-Jensen, D. et al. (2010). “Greenland ice sheet monitoring network (GLISN): a seismological approach”. In: *The Geological Survey of Denmark and Greenland Bulletin* 20.
- Dao, M.H. and P. Tkalich (2007). “Tsunami propagation modelling - a sensitivity study”. In: *Natural Hazards Earth Syst. Science* 7, 741-754.
- Dyson, Freeman (2004). “A meeting with Enrico Fermi”. In: *Nature* 427.
- Echelmeyer, K. et al. (1991). “Surficial glaciology of Jakobshavn Isbræ, West Greenland: Part I. Surface morphology”. In: *Journal of Glaciology* 37.
- Ekstöm, Göran (2006). “Global detection and location of seismic sources by using surface waves”. In: *Bulletin of the Seismological Society of America* 96.

- Ekström, Göran et al. (2003). “Glacial Earthquakes”. In: *Science* 302.
- Elmore, William C. and Mark A. Heald (1969). *Physics of waves*. McGraw-Hill book company.
- Gallotti, G. et al. (2021). “Tsunamis from prospected mass failure on the Marsili submarine volcano flanks and hints for tsunami hazard evaluation”. In: *Bulletin of Volcanology* 93, p. 2. URL: <https://doi.org/10.1007/s00445-020-01425-0>.
- Goto, C. et al. (1997). “Numerical Method of Tsunami Simulation with the Leap-Frog Scheme (IUGG/IOC Time Project)”. In: *IOC Manual* 35.
- Guyon, Etienne et al. (2001). *Physical hydrodynamics*. Oxford university press.
- Heidarzadeh, Mohammad and Kenji Satake (2015). “New Insights into the Source of the Makran Tsunami of 27 November 1945 from Tsunami Waveforms and Coastal Deformation Data”. In: *Pure and Applied Geophysics* 172.
- Heller, Valentin et al. (2019). “Large-scale experiments into the tsunamigenic potential of different iceberg calving mechanisms”. In: *Nature - Scientific Reports* 9.
- Ice Sheet Modeling Group (Department of Earth System Science University of California, Irvine), ed. (2016). *BedMachine Greenland v3*. URL: <https://sites.uci.edu/morlighem/dataproducts/bedmachine-greenland/>.
- Joughin, Ian et al. (2008a). “Ice-front variation and tidewater behavior on Helheim and Kangerdlugssuaq Glaciers, Greenland”. In: *Journal of Geophysical Research: Earth Surface* 113.
- Joughin, Ian. et al. (2008b). “Continued evolution of Jakobshavn Isbræ following its rapid speedup”. In: *Geophysical Research Letters* 32.
- Kawakatsu, Hitoshi (1989). “Centroid single force inversion of seismic waves generated by landslides”. In: *Journal of Geophysical Research: Solid Earth* 94.
- Luckman, Adrian and Tavi Murray (2005). “Seasonal variation in velocity before retreat of Jakobshavn Isbræ, Greenland”. In: *Geophysical Research Letters* 32.
- Lüthi, Martin P. and Andreas Vieli (2016). “Multi-method observation and analysis of a tsunami caused by glacier calving”. In: *The Cryosphere* 10.
- Marchenko, A. V. et al. (2012). “A tsunami wave recorded near a glacier front”. In: *Natural hazards and Earth system science* 12.
- Minowa, Misahiro et al. (2019). “Calving flux estimation from tsunami waves”. In: *Earth and Planetary research letters* 515.
- Motyka, Roman J. et al. (2011). “Submarine melting of the 1985 Jakobshavn Isbræ floating tongue and the triggering of the current retreat”. In: *Journal of Geophysical Research: Earth Surface* 116.
- Mouginot, Jérémie et al. (2019). “Forty-six years of Greenland Ice Sheet mass balance from 1972 to 2018”. In: *Proceedings of the National Academy of Science of the United States of America*.
- Nettles, Meredith and Göran Ekström (2010). “Glacial Earthquakes in Greenland and Antarctica”. In: *Annual Review of Earth and Planetary Sciences* 38.

- Nettles, Meredith et al. (2008). “Step-wise changes in glacier flow speed coincide with calving and glacial earthquakes at Helheim Glacier, Greenland”. In: *Geophysical Research Letters* 35.
- Rignot, Eric and Pannir Kanagaratnam (2006). “Changes in the velocity Structure of the Greenland Ice Sheet”. In: *Science* 311.
- Sergeant, Amandine et al. (2016). “Complex force history of a calving-generated glacial earthquake derived from broadband seismic inversion”. In: *Geophysical Research Letters* 43.
- Spencer, A. J. M. (1980). *Continuum Mechanics*. Mineola (New York): Dover Publications, Inc.
- Stoker, J. J. (1992). *Water waves: the mathematical theory with applications*. Interscience Publishers Inc.
- Sun, Sainan et al. (2017). “Ice shelf fracture parametrization in an ice sheet model”. In: *The Cryosphere Discussions*.
- Thomas, R. et al. (2006). “Progressive increase in ice loss from Greenland”. In: *Geophysical research letters* 33.
- Tinti, Stefano and Roberto Tonini (2013). “The UBO-TSUFDF tsunami inundation model: validation and application to a tsunami case study focused on the city of Catania, Italy”. In: *Natural Hazards and Earth System Sciences* 13.
- Triantafyllou, I. et al. (2020). “The Large Earthquake (M7) and Its Associated Tsunami of 8 November 1905 in Mt. Athos, Northern Greece”. In: *Pure and Applied Geophysics* 117, pp. 1267–1293. URL: <https://doi.org/10.1007/s00024-019-02363-5>.
- Tsai, Victor C. and Göran Ekström (2007). “Analysis of glacial earthquakes”. In: *Journal of Geophysical Research: Earth Surface* 112.
- Tsai, Victor C. et al. (2008). “Possible mechanisms for glacial earthquakes”. In: *Journal of Geophysical research* 113.
- UNESCO, ed. (2021). *Ilulissat Icefjord*. URL: <https://whc.unesco.org/en/list/1149/>.
- Veen, C. J. van der (2002). “Calving glaciers”. In: *Progress in Physical Geography, Earth and Environment* 26.
- Veicht, Stephen A. and Meredith Nettles (2012). “Spatial and temporal variations in Greenland glacial-earthquake activity, 1993–2010”. In: *Journal of Geophysical Research: Earth Surface* 117.
- Velicogna, Isabella and John Wahr (2006). “Acceleration of Greenland ice mass loss in spring 2004”. In: *Nature* 443.
- Walder Joseph S. and Watts, Philip et al. (2003). “Tsunamis generated by subaerial mass flows”. In: *Journal of Geophysical Research: Solid Earth* 108.
- Walter, Fabian et al. (2010). “Iceberg calving during transition from grounded to floating ice: Columbia Glacier, Alaska”. In: *Geophysical Research Letters* 37.

- Walter, Fabian et al. (2012). “Analysis of low-frequency seismic signals generated during a multiple-iceberg calving event at Jakobshavn Isbræ, Greenland”. In: *Journal of Geophysical Research* 117.
- Walter, Fabian et al. (2013). “Calving event detection by observation of seiche effects on the Greenland fjords”. In: *Journal of Glaciology* 213.
- Zaniboni, Filippo et al. (2018). *Calving-induced tsunami analyzed through seismic signals and numerical codes*. Poster presented in Polar 2018, Davos (Switzerland) 19-23 June 2018.
- Zaniboni, Filippo et al. (2021). “Tsunamis From Submarine Collapses Along the Eastern Slope of the Gela Basin (Strait of Sicily)”. In: *Frontiers in Earth Science* 8, p. 602171. URL: <https://doi:10.3389/feart.2020.602171>.